# Chapter 4
# Theoretical Modeling of the Optical and Electrical Processes in Polymeric Solar Cells

**Zhigang Shuai, Lingyi Meng and Yuqian Jiang**

**Abstract** The elementary processes occurred in organic solar cell include optical absorption, excitation energy transfer, photoinduced charge transfer, charge transport, and charge collection at the electrodes. Even though modern quantum chemistry has achieved great success in electronic structure calculations, it is still not enough to describe these elementary processes at first-principles. We describe in this chapter our recent progresses toward quantitative theoretical understanding of the optical and electronic processes in organic photovoltaic materials, including optical absorption and emission spectra for conjugated oligomers, energy transfer in polymers, charge transport in organic semiconductors, and device modeling of heterojunction solar cells based on dynamic Monte Carlo simulation and the continuum model.

## 4.1 Introduction

Elementary electronic processes in organic and polymeric solids have been intensively investigated over the past decades [1, 2]. Carbon atom is the basic element in these materials, where 4 valence electrons form chemical bonds, sigma (σ) or pi (π) bonds, the former forms the skeleton for the conjugated polymer and the latter contributes mostly to the electronic valence and conduction bands. The electronic function comes from the unsaturated π-electron. The prototypical conjugated polymer is polyacetylene with a repeat unit of (CH) group connected alternatively by single and double bond, denoted as $(CH)_N$. Since Heeger, MacDiarmid and

Z. Shuai (✉) · Y. Jiang
MOE Key Laboratory of Organic OptoElectronics and Molecular Engineering, Department of Chemistry, Tsinghua University, 100084 Beijing, China
e-mail: zgshuai@tsinghua.edu.cn

Z. Shuai · L. Meng
Collaborative Innovation Center of Chemistry for Energy Materials, Xiamen University, 361005 Xiamen, China



Y. Yang and G. Li (eds.), *Progress in High-Efficient Solution Process Organic Photovoltaic Devices*, Topics in Applied Physics 130,
DOI 10.1007/978-3-662-45509-8_4

Shirakawa discovered that polyacetylene can be doped to become conducting polymer [3, 4], tremendous efforts have been focused in this field, which led to the discoveries of organic and polymeric nonlinear optical phenomena [5], polymer light-emitting diodes [6] and flexible display [7], polymer lasing [8–10], organic and polymeric field effect transistor [11, 12], chemico- and biosensors [13], and most impressively, polymer solar cells [14] as exclusively discussed in this book. We have gained fundamental understandings of the electronic processes from pi-electron conjugation to Peierls instability in one-dimensional system [15], electron-phonon coupled nonlinear excitations like soliton and polaron [16], structure property relationship for the nonlinear optical response [17]. However, we are still at a stage in debating the nature of the photoexcitation [18] and in improving our understandings of the charge and energy excitation transfer processes [19] as well as electronic structures at various interfaces [20].

Polymer bulk heterojunction structure for solar cells has been proposed for a while [21] which drove the field to a much higher level and the power conversion efficiency has been increased ten-fold during the past decade. However, the more and more complex materials structures have only obscured our fundamental understanding in terms of the elementary processes. Our knowledge on the photoinduced charge generation [22], charge transport mechanism [23], and influences of the various interfaces is quite limited and often quite controversial. This in turn hinders the further improvements of the performances for electronic devices. In this chapter, we do not intend to discuss the controversial issues in this field, even though some progresses have been achieved but without definite answers. Instead, we focus on two subjects which are both important and practical for OPV materials design and device improvement, namely, the first-principles optical absorption and emission spectra calculation and the device modeling.

The optical absorption spectra for conjugated polymer or oligomer have strong impact on the portion of photons absorbed from solar emission. Optical emission after photoexcitation consists of an important factor for excitation energy transfer: in a localized exciton picture, the energy transfer can be simply viewed as emission reabsorption so that the spectra overlap between absorption and emission becomes the Franck-Condon factor for the Förster energy transfer rate. Such rate along with the exciton life time determines the exciton diffusion length, which is general short in conjugated polymers, limiting the power conversion efficiency. We will discuss the theoretical aspects on how to compute the optical absorption and emission spectra as well as excited state life time from first-principles. The next process after exciton migration is the charge generation or charge separation at the micro-interface between donor and acceptor. In general, the photoexcitation forms a bound electron-hole pair, or exciton, useless for electrical current. When such species reach the donor/acceptor interface, hole stays in donor (polymer) and the electron moves to acceptor. This process is extremely fast [24] and very much morphology dependent [25]. Such bound pair, sometimes termed as interchain polaron pair, can contribute to current only after further dissociation, subject to charge recombination for energy loss at the same time. The further charge dissociation process is driven by the internal electric field [26]. There have been

tremendous investigations on the charge transport processes in organic and polymeric materials. Often, phenomenological disorder models, most notably proposed by Bassler [27] and more recently developed by Blom and coworkers [28, 29], have been extensively applied. The fundamental assumptions are that there are considerable amounts of disorders with a Gaussian distributed energy levels and the charge hops through these disordered sites following the Miller-Abraham formalism by the phonon-assisted mechanism. Indeed, through multi-scale first-principles calculation on disordered polymers, Vukmirovic and Wang found that the typical charge mobility ranges $10^{-6}$ to $10^{-4}$ $cm^2/Vs$ [30] and both the temperature and field-strength dependence from such disordered model agree with experiments on polymer electronic device. On another hand, if one views polymer with rigid and regular skeleton, the charge mobility along the conjugation chain direction is usually around a few hundred $cm^2/Vs$ [31]. And if there forms ordered interchain stacking structure at microscale, for instance, for regioregular polythiophene, the charge mobility along the π–π stacking direction has been estimated to be around a few $cm^2/Vs$ from deformation potential theory calculation [32]: earlier experimental results demonstrated that the microscale ordering in polymer can increase the charge mobility from $10^{-6}$ to around $10^{-2}$ to $10^{-1}$ $cm^2/Vs$, opening the door to plastic electronics [33]. However, recent progresses are such fascinating that the charge mobility reaches 1–10 $cm^2/Vs$ [34, 35], challenging our present understanding based on disorders. On another hand, the charge transport in molecular crystals or films field-effect-transistor has become a central issue recent years [23]. Our theoretical understanding has been greatly promoted through first-principles calculation coupled with charge transfer theory or charge diffusion dynamics: now, quantitative prediction of charge mobility for organic materials becomes possible [36, 37]. Since there have been extensive reviews on the charge transport phenomena, [23, 36–39], we will not discuss such issue here, even though, the charge transport within donor-acceptor heterojunction materials is still far from clear.

In this chapter, we discuss two theoretical aspects on organic photovoltaics, one on the optical spectra, absorption and emission, and the excited state lifetime, which are closely correlated with exciton diffusion length, and another on the device modeling either from dynamic Monte Carlo simulation and continuum device model.

## 4.2 Optical Properties of Conjugated Polymers: Parameters for Determining the Exciton Diffusion

Optical property of conjugated polymers consists of optical absorption and emission, optical excitation and decay lifetime, as well as excitation energy transfer, each of which is essential to photovoltaic process. The exciton diffusion length is expressed as $L_{ex} = \sqrt{ZD\tau}$, where Z is a constant related to spatial dimension of random walk and τ is the exciton lifetime $\tau = 1/(k_r + k_{nr})$, $k_r$ and $k_{nr}$ are radiative and non-radiative decay rates. Under the hopping picture, the diffusion coefficient $D$ can

be approximated as $D = a^2 k_{et}$, where $a$ is the intersite spacing. In Förster energy transfer model, $k_{et}$ is determined by the overlap between the emission and the absorption spectrum times the intermolecular electronic coupling term for exciton. Long exciton diffusion length means efficient charge dissociation. Thus, polymer emission and absorption spectra as well as exciton decay rates are essential for determining the solar cell performance.

### 4.2.1 First-Principles Calculations of Optical Absorption and Emission Spectra

The optical absorption is described by the absorption cross section, defined as the rate of photon energy absorbed per molecule per unit radiant energy flux,

$$\sigma_{\text{abs}}(\omega) = \frac{4\pi^2\omega}{3c}\sum_{v_i,v_f} P_{iv_i}(T)\left|\left\langle \Theta_{fv_f}\left|\vec{\mu}_{fi}\right|\Theta_{iv_i}\right\rangle\right|^2 \delta\left(\hbar\omega - E_{fi} - E_{fv_f} + E_{iv_i}\right) \tag{4.1}$$

and inversely, the emission spectrum is defined as the differential spontaneous photon emission rate per molecule per unit frequency at ω

$$\sigma_{\text{em}}(\omega) = \frac{4\omega^3}{3c^3}\sum_{v_i,v_f} P_{iv_i}(T)\left|\left\langle \Theta_{fv_f}\left|\vec{\mu}_{fi}\right|\Theta_{iv_i}\right\rangle\right|^2 \delta\left(E_{if} + E_{iv_i} - E_{fv_f} - \hbar\omega\right) \tag{4.2}$$

Here we apply the Born–Oppenheimer approximation, vibronic states $|\Psi_{iv_i}\rangle$ and $|\Psi_{fv_f}\rangle$ are described by the products of the electronic states $|\Phi_i\rangle$, $|\Phi_f\rangle$ and the vibrational states $|\Theta_{iv_i}\rangle$, $|\Theta_{fv_f}\rangle$; $i$ and $f$ are labels of the initial and the final electronic states, respectively, and the corresponding vibrational quantum numbers are denoted by $v_i$ and $v_f$. $P_{iv_i}(T)$ is the Boltzmann distribution function for the initial vibronic manifold. $\vec{\mu}_{fi} = \langle \Phi_f|\vec{\mu}|\Phi_i\rangle$ is the electric transition dipole moment: the interaction between light and molecule is described by the electric dipole approximation and the weak field limit (first-order perturbation). Around the equilibrium geometry, the vibrational states are given by the harmonic oscillator in the normal mode coordinate space. In general, the molecular ground state and the electronically excited state possess different potential energy surfaces. Namely, the vibrational frequency can be different even for the same mode. Since the transition moments in (4.1) and (4.2) should be evaluated in the same space, it is convenient to relate the two coordinate spaces through the Duschinsky rotation matrix:

$$Q_{ik} = \sum_{l}^{N} S_{i\leftarrow f,kl} Q_{fl} + \underline{D}_{i\leftarrow f,k} \tag{4.3}$$

where $Q_{ik}$ is the vibrational coordinate for $k$th mode of the initial state, $S$ is the Duschinsky rotation matrix and $D$ is a the displacement vector connecting the minima of the two parabolas. That is, any one vibrational state vector in the initial (final) parabola can be regarded as a linear combination of all the vectors in the final (initial) parabola plus a rigid shift in origin, see Scheme 4.1. In addition, the electric dipole transition moment depends on the vibrational coordinate:

$$\vec{\mu}_{fi} = \vec{\mu}_0 + \sum_k \vec{\mu}_k Q_k + \sum_{k,l} \vec{\mu}_{kl} Q_k Q_l + \cdots \tag{4.4}$$

where the first term is coordinate independent, which is enough for strongly dipole allowed transition (Franck-Condon approximation, FC), the second term is the first-order expansion in the Taylor series (Herzberg-Teller term, HT). Substituting (4.4) into (4.1) and (4.2), and then Fourier transforming the delta-function, the optical spectrum function can be recast into the following forms (taking emission as example):

$$\sigma_{\mathrm{em}}(\omega) = \sigma_{\mathrm{em}}^{\mathrm{FC}}(\omega) + \sigma_{\mathrm{em}}^{\mathrm{FC/HT}}(\omega) + \sigma_{\mathrm{em}}^{\mathrm{HT}}(\omega) \tag{4.5}$$

$$\sigma_{\mathrm{em}}^{\mathrm{FC}}(\omega) = \frac{2\omega^3}{3\pi\hbar c^3} |\vec{\mu}_0|^2 \int_{-\infty}^{\infty} \mathrm{e}^{-i(\omega-\omega_{if})t} Z_{iv}^{-1} \rho_{\mathrm{em},0}^{\mathrm{FC}}(t,T)\mathrm{d}t \tag{4.6}$$

$$\sigma_{\mathrm{em}}^{\mathrm{FC/HT}}(\omega) = \frac{2\omega^3}{3\pi\hbar c^3} \sum_k \vec{\mu}_0 \cdot \vec{\mu}_k \int_{-\infty}^{\infty} \mathrm{e}^{-i(\omega-\omega_{if})t} Z_{iv}^{-1} \rho_{\mathrm{em},k}^{\mathrm{FC/HT}}(t,T)\mathrm{d}t \tag{4.7}$$

$$\sigma_{\mathrm{em}}^{\mathrm{HT}}(\omega) = \frac{2\omega^3}{3\pi\hbar c^3} \sum_{k,l} \vec{\mu}_k \cdot \vec{\mu}_l \int_{-\infty}^{\infty} \mathrm{e}^{-i(\omega-\omega_{if})t} Z_{iv}^{-1} \rho_{\mathrm{em},kl}^{\mathrm{HT}}(t,T)\mathrm{d}t \tag{4.8}$$

where $Z_{iv}$ is the partition function, and

$$\rho_{\mathrm{em},0}^{\mathrm{FC}}(t,T) = \mathrm{Tr}\left[\mathrm{e}^{-i\tau_f \hat{H}_f} \mathrm{e}^{-i\tau_i \hat{H}_i}\right] \tag{4.9}$$

$$\rho_{\mathrm{em},k}^{\mathrm{FC/HT}}(t,T) = \mathrm{Tr}\left[Q_{fk} \mathrm{e}^{-i\tau_f \hat{H}_f} \mathrm{e}^{-i\tau_i \hat{H}_i}\right] \tag{4.10}$$

$$\rho_{\mathrm{em},kl}^{\mathrm{HT}}(t,T) = \mathrm{Tr}\left[Q_{fk} \mathrm{e}^{-i\tau_f \hat{H}_f} Q_{fl} \mathrm{e}^{-i\tau_i \hat{H}_i}\right] \tag{4.11}$$

are the three kinds of thermal vibration correlation functions. $\tau_f = t/\hbar$, $\tau_i = -i\beta - \tau_f$, and $\beta = (k_{\mathrm{B}}T)^{-1}$. Within the multi-dimensional harmonic oscillator model, (4.9–4.11) can be evaluated analytically with consideration of Duschinsky rotation effect [40, 41] and Herzberg-Teller [42]. All the quantities appeared in the

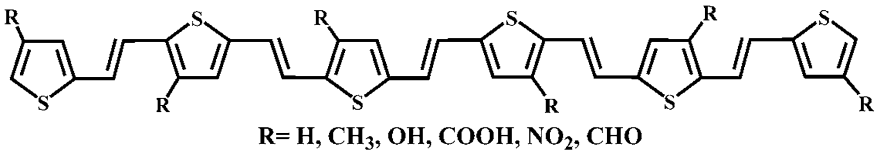


**Scheme 4.1** Molecular structure of pristine and substituted PTV oligomers

formalisms can be obtained by modern quantum chemistry, such as vertical and adiabatic electronic excitation energies, vibrational frequency and normal modes at both ground state and excited state, transition electrical dipole moment and its first-order derivative with respect to normal mode. Duschinsky rotation matrix and the displacement vector appeared in (4.3) can be obtained by putting the ground state and the excited state molecular geometries in one common reference frame according to translational and rotational Eckart conditions [43].

### *4.2.2 Excited State Decay Rate: Radiative and Non-radiative*

According to the Jablonski diagram, there are three main decay pathways from the lowest photoexcited state $S_1$ to the ground state: (i) the radiative decay from $S_1$ to $S_0$; (ii) the non-radiative internal conversion (IC) from $S_1$ to $S_0$ with a rate $k_{IC}$; (iii) the intersystem crossing (ISC) process from $S_1$ to the first triplet excited state ($T_1$) with a rate $k_{ISC}$.

The radiative decay rate can be simply expressed as the integration over the wavelength of the light emission spectrum:

$$k_r(T) = \int_0^\infty \sigma_{emi}(\omega, T) d\omega \tag{4.12}$$

The IC rate can be evaluated through Fermi's golden rule presented as:

$$k_{IC} = \frac{2\pi}{\hbar} \left| H'_{fi} \right|^2 \delta\left(E_{fi} + E_{fv_f} - E_{iv_i}\right) \tag{4.13}$$

Here the perturbation is the non-Born-Oppenheimer coupling:

$$H'_{fi} = -\hbar^2 \sum_l \left\langle \Phi_f \Theta_{fv_f} \left| \frac{\partial \Phi_i}{\partial Q_{fl}} \frac{\partial \Theta_{iv_i}}{\partial Q_{fl}} \right\rangle \right. \tag{4.14}$$

Under Condon approximation, (4.14) is evaluated as

$$H'_{fi} = \sum_{l} \langle \Phi_f | \hat{P}_{fl} | \Phi_i \rangle \langle \Theta_{fv_f} | \hat{P}_{fl} | \Theta_{iv_i} \rangle \tag{4.15}$$

Here, $\hat{P}_{fl} = -i\hbar \frac{\partial}{\partial Q_{fl}}$ is the normal mode momentum. Inserting (4.15) into (4.13), the IC rate becomes

$$k_{IC} = \sum_{kl} k_{ic,kl} \tag{4.16}$$

$$k_{ic,kl} = \frac{2\pi}{\hbar} R_{kl} Z_{iv}^{-1} \sum_{v_i, v_f} \mathrm{e}^{-\beta E_{iv_i}} P_{kl} \delta\left(E_{fi} + E_{fv_f} - E_{iv_i}\right) \tag{4.17}$$

Here electronic coupling term

$$R_{kl} = \langle \Phi_f | \hat{P}_{fk} | \Phi_i \rangle \langle \Phi_i | \hat{P}_{fl} | \Phi_f \rangle \tag{4.18}$$

and vibrational coupling term

$$P_{kl} = \langle \Theta_{fv_f} | \hat{P}_{kl} | \Theta_{iv_i} \rangle \langle \Theta_{iv_i} | \hat{P}_{fl} | \Theta_{fv_f} \rangle \tag{4.19}$$

The delta function in (4.17) is again Fourier transformed which gives rise to:

$$k_{ic,kl} = \frac{1}{\hbar^2} R_{kl} \int_{-\infty}^{\infty} dt \left[ \mathrm{e}^{i\omega_{if} t} Z_{iv}^{-1} \rho_{ic,kl}(t, T) \right] \tag{4.20}$$

where $\rho_{ic,kl}(t, T) = \mathrm{Tr}\left( \hat{P}_{fk} \mathrm{e}^{-i\tau_f \hat{H}_f} \hat{P}_{fk} \mathrm{e}^{-i\tau_i \hat{H}_i} \right)$ is the IC correlation function, for which, Peng et al. [44] derived the analytical expression for diagonal case ($k = l$) and Niu et al. [45] obtained more general expression for both diagonal and non-diagonal couplings, thus completely abandoning the "promoting mode" approximation. Namely, any vibrational mode could serve as a promoting mode for the internal conversion process. It can be applied to complex molecules. The electronic coupling appeared in (4.18) is also termed as non-adiabatic coupling, which can be obtained through first-order perturbation [46]:

$$\langle \Phi_f | \frac{\partial}{\partial Q_{fl}} | \Phi_i \rangle = \frac{\left\langle \Phi_f^0 \middle| \partial V / \partial Q_{fl} \middle| \Phi_i^0 \right\rangle}{E_i^0 - E_f^0} \tag{4.21}$$

where V is the electron-nuclear interaction term in Hamiltonian, and the numerator can be expressed as a sum over transition electric field from nucleus:

$$\left\langle \Phi_f^0 \middle| \partial V/\partial Q_{fl} \middle| \Phi_i^0 \right\rangle = -\sum_{\sigma} \frac{Z_\sigma e^2}{\sqrt{M_\sigma}} \sum_{\tau=x,y,z} E_{f\leftarrow i,\sigma\tau} L_{\sigma\tau} \tag{4.22}$$

where

$$E_{f\leftarrow i,\sigma\tau} = \int \mathrm{d}\mathbf{r} \rho_{fi}(\mathbf{r}) \frac{e(r_\tau - R_{\sigma\tau})}{|\mathbf{r} - \mathbf{R}_\sigma|^3}$$

is the electric field at $\mathbf{r}$ from the a nucleus at $\mathbf{R}_\sigma$ and $\rho_{fi}$ is the electron transition density between initial and final states. All can be computed from quantum chemistry program.

### 4.2.3 Application to Polythienylenevinylene Derivatives

As an example to apply the above formalisms to design polymeric photovoltaic materials, we consider polythienylenevinylene (PTV) derivatives. In fact, the most prominent polymer for photovoltaic application has been poly(3-hexyl thiophene) (P3HT), which when processed with P3HT to form bulk heterojunction structure can give rise up to 6 % power conversion efficiency [47]. The band gap of P3HT is 2 eV, much higher than the silicon band gap 1.1 eV. One of the recent developments towards reaching higher efficiency is to synthesize low band gap polymer to absorb as much as possible solar emissions, for instance, the intra-chain donor-acceptor backbone polymers or copolymers [48]. One strategy to lower the band gap of polythiophene is to consider polythienylvinylene, see Scheme 4.1. The band gaps of PTV and its derivatives are around 1.55–1.8 eV. However, the pristine PTV was shown to possess very low power conversion efficiency, $\sim$0.2 % [49], regardless of the improved absorption spectrum and large charge mobility. It has been observed that the photo-induced transfer from PTV to PCBM is very low and the excited state decay is very fast (0.6 ps) [50], instead of nanoseconds. Such fast non-radiative decay prohibits any appreciable fluorescence. In fact, there is a concomitant relationship between fluorescence and photovoltaic process: the former is necessary for excitation energy transfer prior to charge separation.

Further experiments have been devoted to make substituted PTV in order to increase the power conversion efficiency. One strategy is to increase optical emission efficiency, which is much easier to characterize without fabricating device. It has been known that the absence of photoluminescence is due the lowest-excited state ordering, commonly occurred in conjugated polymer, like polyacetyelene, or polydiacetylene [51]. Namely, the lowest excited state is of even parity, dipole-forbidden, often $2A_g$ state, while for the luminescent polymer like polyparaphenylenevinylene (PPV), it is of odd parity, dipole-allowed $1B_u$ state [52]. It has been demonstrated that upon side-chain substitutions, the luminescence can be recovered through $1B_u/2A_g$ crossover [53, 54]. The side-chain substitution can cause the

main-chain charge redistribution at the frontier molecular orbital and stabilize the charge-type excitation ($1B_u$ state). Theoretically, the substitution effect on the lowest-lying excited state ordering is very difficult to predict, since quantum chemistry so far does not allow accurate calculation of the excited state for large molecules. Complete active space self-consistent field plus its second order perturbation (CASPT2) can provide a rather reliable description for low-lying excited states [55]. However, the computational costs usually prohibit any computational efforts for complex conjugated oligomers or polymers. We have earlier improved semiempirical ZINDO coupled with multireference configuration interaction (MRCI/ZINDO) approach to calculate the excited state and nonlinear optical properties for conjugated molecules, which has been shown to give reliable low-lying excited state structure [56, 57]. Furthermore, Chen et al. [56] proposed a simple rule to judge the substitution effect on the crossover of the excited state ordering based on frontier molecular orbitals, which is practical for luminescent polymer design. The following quantity $\rho_{H/L}$ is defined:

$$\rho_{\frac{H}{L}} = \frac{\sum_{\mu \in sub} \left| C_{H_\mu} \right|^2}{\sum_{\mu \in sub} \left| C_{L_\mu} \right|^2}$$

$C_{H(L)}$ is the molecular orbital coefficient of the HOMO(LUMO) at the substitution site of the main chain, and the summations only cover the orbitals of the carbon atoms in the backbone linking the side groups. Therefore, $\rho_{H/L}$ can mark charge redistribution between the HOMO and LUMO induced by substituent groups. Since $1B_u$ usually consists of single excitation from HOMO to LUMO, charge transfer occurring from HOMO to LUMO should be significant to stabilize the $1B_u$ state. If $\rho_{H/L}$ deviates from 1 remarkably, charge transfer from substituent group to the main chain will occur upon excitation from HOMO to LUMO, so that the $1B_u$ can be stabilized to become the lowest-lying excited state. Otherwise, if $\rho_{H/L}$ is close to 1, then the excited state ordering is not expected to be altered upon substitution.

The regioregular PTVs at solid state possess planar conformation, leading to highly conjugated backbones. Therefore, the model systems are kept planar with $C_{2h}$ symmetry in this work. Based on the $S_0$ geometries optimized by B3LYP/def2-SV(P), the vertical excitation energies of the three low-lying excited states for the six PTV derivatives (Scheme 4.1) are calculated with TDDFT/B3LYP and MRCI/ZINDO methods, and the results are presented in Table 4.1 [58].

It is noted that (i) for the pristine and $CH_3$-, OH- substituted PTV, the lowest excited state is of $A_g$ symmetry, prohibiting any appreciable fluorescence according to Kasha's rule; (ii) both $NO_2$- and CHO substitution can alter the excited state ordering thus to recover the fluorescence; (iii) TDDFT/B3LYP method always stabilizes the $1B_u$ state to be the lowest one. This is due to the artefact of the charge self-interaction contained in the functional. Several recent efforts have tried to correct such mistakes, including spin-flip approach [59], non-adiabatic effect [60], double-excitation [61], etc. These are in active progress. The MRCI/ZINDO calculated excited state structure correlated well with $\rho_{H/L}$ value from the simple rule

**Table 4.1** Vertical excitation energies ($E_{ver}$) of the three low-lying excited states at the ground state geometry for PTV derivatives and their corresponding oscillator strengths (f)

| | MRCI/ZINDO | | TDDFT/B3LYP | |
|---|---|---|---|---|
| R | $E_{vert}$ (eV) | f | $E_{vert}$ (eV) | f |
| H | $A_g$: 2.50 | 0.0000 | $B_u$: 1.94 | 3.9113 |
| | $B_u$: 2.76 | 3.1055 | $A_g$: 2.28 | 0.0000 |
| | $A_g$: 3.18 | 0.0000 | $A_g$: 2.66 | 0.0000 |
| $CH_3$ | $A_g$: 2.51 | 0.0000 | $B_u$: 1.93 | 3.9387 |
| | $B_u$: 2.73 | 2.9759 | $A_g$: 2.28 | 0.0000 |
| | $A_g$: 3.12 | 0.0000 | $A_g$: 2.64 | 0.0000 |
| OH | $A_g$: 2.38 | 0.0000 | $B_u$: 1.75 | 3.5981 |
| | $B_u$: 2.41 | 2.2482 | $A_g$: 2.03 | 0.0000 |
| | $A_g$: 2.89 | 0.0000 | $A_g$: 2.55 | 0.0000 |
| CO-OH | $B_u$: 2.41 | 3.3457 | $B_u$: 2.03 | 3.3678 |
| | $A_g$: 2.58 | 0.0000 | $A_g$: 2.32 | 0.0000 |
| | $A_g$: 2.83 | 0.0000 | $A_g$: 2.58 | 0.0000 |
| $NO_2$ | $B_u$: 2.45 | 3.0844 | $B_u$: 2.03 | 2.9424 |
| | $A_g$: 2.55 | 0.0000 | $A_g$: 2.24 | 0.0000 |
| | $A_g$: 2.84 | 0.0000 | $A_g$: 2.51 | 0.0000 |
| CH-O | $B_u$: 2.38 | 3.2248 | $B_u$: 1.96 | 3.1874 |
| | $A_g$: 2.51 | 0.0000 | $A_g$: 2.21 | 0.0000 |
| | $A_g$: 2.77 | 0.0000 | $A_g$: 2.49 | 0.0000 |

based on the molecular orbital analysis, as well as the available experiments, see Table 4.2.

If we look at the frontier orbitals of these compounds, see Fig. 4.1, we can see that for $CH_3$-substitution does not alter the charge distribution when compared with pristine one, while OH-substitution can indeed redistribute orbital, but it does so both to HOMO and LUMO in a very similar way. COOH, $NO_2$ and CHO substituents are strongly electron-withdrawing groups, and they all caused remarkable charge redistributions, especially in LUMO. That explains that $CH_3$ and OH substitutions cannot give rise to fluorescence but COOH, $NO_2$ and CHO can. Indeed, experiment indicated COOH-PTV is light-emissive and its photovoltaic efficiency has been increased 10 times from pristine polymer [63].

Now we look at the optical spectra for the three compounds predicted to be emissive. TDDFT/B3LYP is employed to calculate all the vibrational modes for

**Table 4.2** Calculated $\rho_{H/L}$ from the optimized geometry for different substituted OTVs, in comparison with the MRCI/ZINDO results and experimental luminescent properties: strong luminescent molecules possess a $\rho_{H/L}$ value well deviated from 1

| R | H | $CH_3$ | OH | COOH | $NO_2$ | CHO |
|---|---|---|---|---|---|---|
| $\rho_{H/L}$ | 1.29 | 1.20 | 0.91 | 1.51 | 1.40 | 1.85 |
| $S_1$ from MRCI/ZINDO | $2A_g$ | $2A_g$ | $2A_g$ | $1B_u$ | $1B_u$ | $1B_u$ |
| Luminescence from exp. | No [62] | No [63] | No [50] | *Yes* [63] | NA | NA |

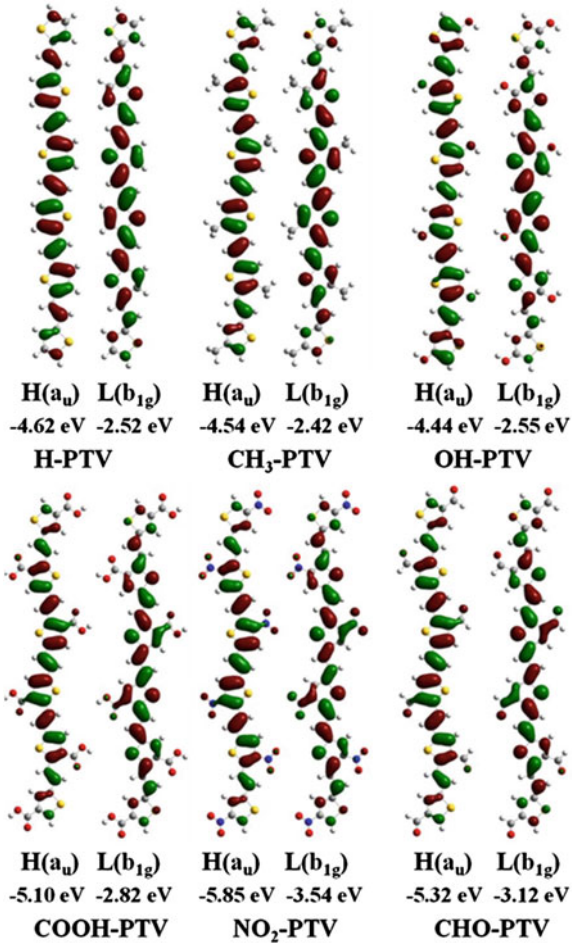


**Fig. 4.1** Frontier orbitals of PTV: H for HOMO and L for LUMO

excited state and the ground state as well as the vibronic coupling. Keeping in $C_{2h}$ symmetry, no imaginary frequency is found from the optimized ground state structure for all three PTVs, indicating local minimums are located. While there is a very small imaginary frequency existed in optimized excited state structure for COOH-PTV and $NO_2$-PTV, no matter by keeping $C_{2h}$ symmetry or $C_1$ symmetry. Such mode corresponds to the slight out-of plane motion with vanishing vibronic coupling strength. Thus, it is safe to replace such mode by the corresponding one in the ground state, ignoring the distortion effect for this particular mode.

We first present the absorption and emission spectra for the experimentally available COOH-PTV at 300 K including Duschinsky effect in order to rationalize our methodology. The theoretical spectra compared with the experimental results [63] are presented in Fig. 4.2, which is quite satisfactory. Note that the broadening in spectrum is naturally temperature dependent, originated from the coupling

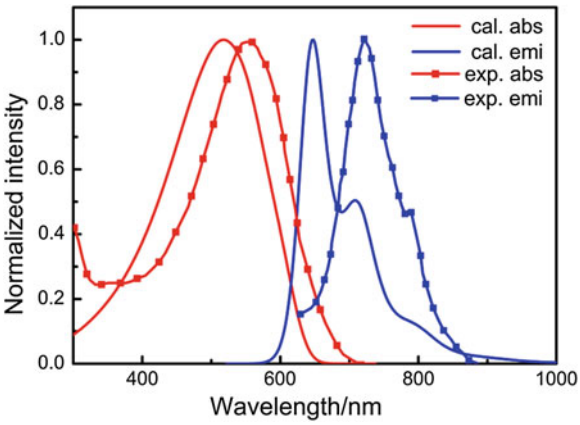


**Fig. 4.2** Comparison of optical absorption and emission spectra between theory (T = 300 K) and experiment (in dilute $CHCl_3$ solution) for COOH-PTV

between electronic excited state and all the vibration modes, without any arbitrary broadening. We find the line shapes in theoretical spectra are in good agreement with the experiment. Such agreement validates our vibration correlation function theory and the electronic structure calculation.

Under the displaced harmonic oscillator model, there should exist mirror symmetry between the absorption and emission spectra. But such symmetry is absent both in experiment and in theory, see Fig. 4.2. To understand the origin of such asymmetry, we calculate the spectra without considering the mode mixing effect, while keeping the difference in normal mode frequency between excited state and ground state as obtained from TDDFT (Fig. 4.3). And we find that the structures of spectra are nearly the same as the spectra with Duschinsky rotation effect (DRE) and the asymmetry still exists. This means the mixing of normal modes in the initial and final electronic states is not the cause of asymmetry. Therefore, the asymmetry of spectra can be ascribed to the distortion effect. Such asymmetry also existed in

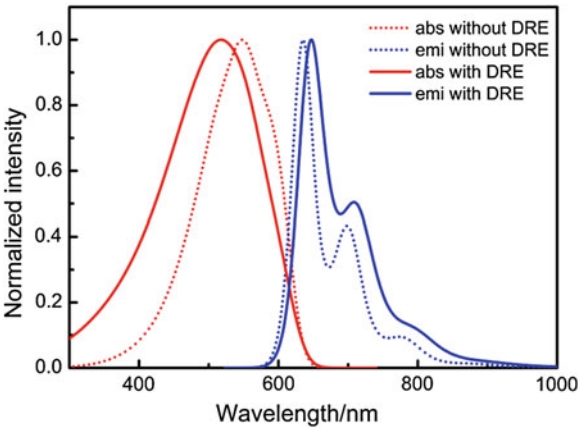


**Fig. 4.3** The optical absorption (abs) and emission (emi) spectra of COOH-PTV with DRE compared to the spectra without DRE but with different normal mode frequency at 300 K

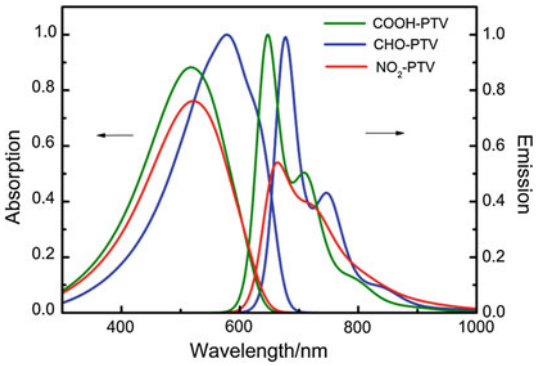


**Fig. 4.4** Theoretical absorption and emission spectra for COOH-PTV, $NO_2$-PTV, and CHO-PTV

polythiophene and polyparaphenylenevinylene [64], because in the excited state, C–C single bond is shortened so that the frequency of torsional motion increases.

We next calculate the optical spectra of $NO_2$-PTV and CHO-PTV, shown in Fig. 4.4. The absorptions peak at 518, 522, 578 nm for COOH-PTV, $NO_2$-PTV, and CHO-PTV respectively, while for emission, the peak positions are at 648, 663, and 678 nm correspondingly. The bandgap of CHO-PTV is indeed much lower than other compounds. The theoretical spectra illustrate that CHO-PTV possesses a large overlap between absorption and emission spectra, helpful for faster energy transfer. Thus, we conclude that CHO-PTV possesses the smallest bandgap as well as the largest spectra overlap.

Now we look at the excited state decay rates calculated according to formalisms (4.12) and (4.20), see Table 4.3. The exciton life time is simply calculated as $\tau = \frac{1}{k_r + k_{nr}}$. It is seen that all of the three compounds possess efficient fluorescence ($k_r \gg k_{nr}$) as well as long exciton lifetime to facilitate charge dissociation.

It should be noted that in our vibration correlation function formalism, harmonic potential energy surface approximation is adopted, which could be a strong approximation, especially for small molecule with very few degrees of freedom and a large electronic transition gap. For radiative decay process, the transition energy is largely mediated by the photon energy, leaving the vibrational quanta very small. In nonradiative decay, the electronic energy of excited state is transformed through vibration relaxation into final state. If the number of modes is too few and/or the transition energy is too large, the number of vibration quanta for each mode is required to be big in order to accept the electronic energy. As a result, the anharmonicity can be important in the nonradiative decay process. However, if the number of normal modes is large enough, for instance in conjugated polymers, then

**Table 4.3** Radiative, nonradiative decay rates and exciton life time for the emissive substituted PTVs

| R | COOH | $NO_2$ | CHO |
|---|---|---|---|
| $k_r/s^{-1}$ | $5.25 \times 10^8$ | $3.94 \times 10^8$ | $4.50 \times 10^8$ |
| $k_{nr}/s^{-1}$ | $1.19 \times 10^6$ | $2.24 \times 10^8$ | $2.51 \times 10^6$ |
| $\tau$/ns | 1.90 | 1.62 | 2.21 |

many modes can take part in sharing the electronic transition energy. Thus for any one of the mode, only small number of vibrational quanta is required. So, for each mode, the deviation from the potential energy surface equilibrium is small and the harmonic model is expected to be a reasonable approximation. Hence, we expect that the harmonic model is more applicable for polymer than for molecule. Detailed verification can be found in [58].

### *4.2.4 Synopsis*

In this section, we present a general formalism for calculating the optical absorption and emission spectra as well as the excited state decay rates. The material design strategy has been proposed on increasing fluorescence quantum efficiency, due to the concomitant relationship between light-emitting and photovoltaics. Taking polythienylenevinylene as example, which is non-emissive and of low power conversion efficiency, we applied a combined quantum chemistry approach to propose theoretical design strategy to improve the optoelectronic property of PTV. We showed that COOH group substitution in PTV can lead to invert the excited state ordering, allowing light-emitting, but $CH_3$ and OH groups do not cause any appreciable effect. We predict that the electron-withdrawing groups $NO_2$ and CHO can make PTV light-emitting, much as COOH group. These results are further confirmed by molecular orbital calculations based on a simple rule for substitution effect on the excited state ordering, namely, substitution should cause charge redistribution amongst HOMO and LUMO in order stabilize the light-emitting state $1B_u$ to be the lowest one.

Starting from the lowest excited state and the ground state potential energy parabola, optical absorption and emission spectra are computed for COOH-, $NO_2$- and CHO-PTV through our correlation function formalism. The broken mirror symmetry for COOH-PTV found both in experiment and computation is attributed to distortion effect, namely, the vibrational mode frequencies, especially the low frequency parts are different for the ground state and the excited state. The theoretical spectra of COOH-PTV are consistent with the experimental measurements. From the radiative and non-radiative decay rates for COOH-, CHO- and $NO_2$-PTVs as computed by the same correlation function formalism, we find that CHO-PTV possesses not only a long excited state lifetime (2.21 ns), but also large overlap between absorption and emission spectra. These facts indicate that CHO-PTV is not only a good light-emitting polymer, but also a good photovoltaic donor material possessing long intrinsic exciton diffusion length. Although $NO_2$ is a stronger electron-withdrawing group than COOH or CHO, the calculations show that the spectrum overlap between absorption and emission in $NO_2$-PTV is relatively small. Therefore, even though the excited state ordering of $NO_2$-PTV meets the basic requirement for molecular design, both the light emitting and photovoltaic performances are predicted to be poorer than COOH-PTV, while CHO-PTV is predicted to present better light emitting and photovoltaic performances than

COOH-PTV. Such theoretical information should be useful for materials design and the methodology presented in this section is ready to be employed by any graduate students.

Following the photo-absorption and exciton diffusion/dissociation, the next important step is the charge transfer and charge transport. We refer to a monograph for describing such process [65, 66].

## 4.3 Molecular Parameters for Exciton Transfer in Organic Semiconductors

As long as the exciton diffusion length is concerned, apart from the spectra overlap extensively discussed in previous section, intermolecular excitonic/electronic coupling is the central parameter. The microscopic origin comes from the long range Coulomb interaction. Namely, excitation in one molecule, or a chromophore, or a conjugated segment travels to other place through transition electrical dipole coupling.

For the singlet-singlet energy transfer (ET) process in a dimer,

$$^1D^* + {}^1A \rightarrow {}^1D + {}^1A^* \tag{4.23}$$

The electronic coupling of ET can be simply expressed by a first-order perturbation from the product state of donor and acceptor wave functions:

$$V_{DA} = \langle \psi_{D^*}\psi_A | H_{DA} | \psi_D \psi_{A^*} \rangle \tag{4.24}$$

where $H_{DA}$ is the perturbation describing the donor-acceptor interaction. Considering $|\psi_D\rangle$, $|\psi_A\rangle$ as the Hartree-Fock self-consistent-field ground-state determinant, the singlet excited state wave functions can be written approximately as a spin-adapted configuration interaction (CI) form:

$$|\psi_{D^*}\rangle = \frac{1}{\sqrt{2}} \sum_{i_D a_D} Z_{i_D a_D}^{D^*} (a_{D\uparrow}^+ i_{D\uparrow} + a_{D\downarrow}^+ i_{D\downarrow}) |\psi_D\rangle \tag{4.25}$$

$$|\psi_{A^*}\rangle = \frac{1}{\sqrt{2}} \sum_{i_A a_A} Z_{i_A a_A}^{A^*} (a_{A\uparrow}^+ i_{A\uparrow} + a_{A\downarrow}^+ i_{A\downarrow}) |\psi_A\rangle \tag{4.26}$$

$a_{D\uparrow}^+ [i_{D\uparrow}]$ creates an electron with spin up on unoccupied molecular orbital (MO) $a$ (annihilates an electron with spin up on occupied MO $i$), and $Z_{i_D a_D}^{D^*}$, $Z_{i_A a_A}^{A^*}$ are the CI expansion coefficients associated with the $i \rightarrow a$ single excitation. So (4.24) can be rewritten as

$$V_{DA} = \frac{1}{2}\sum_{i_D a_D} Z^{D^*}_{i_D a_D} \sum_{i_A a_A} Z^{A^*}_{i_A a_A} \langle \psi_D \psi_A | (i^+_{D\uparrow} a_{D\uparrow} + i^+_{D\downarrow} a_{D\downarrow}) H_{DA} (a^+_{A\uparrow} i_{A\uparrow} + a^+_{A\downarrow} i_{A\downarrow}) | \psi_D \psi_A \rangle \tag{4.27}$$

The general intermolecular interaction can be written in the second quantization form:

$$H_{DA} = \sum_{pq} h_{pq} p^+ q + \frac{1}{2}\sum_{pqrs} \langle pq|rs\rangle p^+ q^+ sr \tag{4.28}$$

where

$$\begin{aligned} h_{pq} &= \int \phi^*_p(1)(T + V^{ele-nuc})\phi_q(1)\mathrm{d}\vec{r}_1 \\ \langle pq|rs\rangle &= \int \phi^*_p(1)\phi^*_q(2)\frac{1}{r_{12}}\phi_r(1)\phi_s(2)\mathrm{d}\vec{r}_1 d\vec{r}_2 \end{aligned} \tag{4.29}$$

where spin-orbital indices $p$, $q$, $r$, $s$ in each term should contain mixed D and A. Equation (4.27) can finally be expressed as

$$V_{DA} = \sum_{i_D a_D} Z^{D^*}_{i_D a_D} \sum_{i_A a_A} Z^{A^*}_{i_A a_A} [2(a_D i_D | i_A a_A) - (a_D a_A | i_A i_D)] \tag{4.30}$$

$(a_D i_D | i_A a_A) = \int \phi^*_{a_D}(1)\phi_{i_D}(1)\frac{1}{r_{12}}\phi^*_{i_A}(2)\phi_{a_A}(2)dr_1 dr_2$ is the two-electron Coulombic interaction, while $(a_D a_A | i_A i_D)$ is exchange interaction. The former can be two-center integral, which is of long range character, namely, one electron in D and another in A. The latter is a four-center integral, namely, intermolecular bond-bond correlation term, which decays exponentially with the intermolecular distance, thus negligible for long range energy transfer.

For the triplet-triplet energy transfer,

$$^3D^* + {}^1A \rightarrow {}^1D + {}^3A^* \tag{4.31}$$

We have:

$$V_{DA} = \frac{1}{2}\sum_{i_D a_D} Z^{D^*}_{i_D a_D} \sum_{i_A a_A} Z^{A^*}_{i_A a_A} \langle \psi_D \psi_A | (i^+_{D\uparrow} a_{D\uparrow} - i^+_{D\downarrow} a_{D\downarrow}) H_{DA} (a^+_{A\uparrow} i_{A\uparrow} - a^+_{A\downarrow} i_{A\downarrow}) | \psi_D \psi_A \rangle \tag{4.32}$$

It can be shown that the Coulombic terms cancel, leaving only the exchange term:

$$V_{DA} = -\sum_{i_D a_D} Z^{D^*}_{i_D a_D} \sum_{i_A a_A} Z^{A^*}_{i_A a_A} (a_D a_A | i_A i_D) \tag{4.33}$$

It demonstrates that only the short-range exchange interaction determines the triplet-triplet energy transfer, which was referred to Dexter mechanism. Here we will not consider this. Only Förster model will be discussed in this chapter.

The intermolecular coupling term can be cast into a practical form by expanding the $1/r_{12}$ in the Coulomb term:

$$\frac{1}{r_{12}} = \frac{1}{|\vec{R}_{DA} + \vec{r}_{A2} - \vec{r}_{D1}|} = \frac{1}{\sqrt{R^2_{DA} + 2\vec{R}_{DA} \cdot (\vec{r}_{A2} - \vec{r}_{D1}) + (\vec{r}_{A2} - \vec{r}_{D1})^2}} \tag{4.34}$$

where $R_{DA}$ is the donor—accepter intercenter distance, $r_{D1}$ the coordinate of electron 1 with respect to the center of donor. Since the latter is much less than the former, $1/r_{12}$ can be expanded:

$$\frac{1}{r_{12}} = \frac{1}{R_{DA}}\left[1 - \frac{\vec{R}_{DA} \cdot (\vec{r}_{A2} - \vec{r}_{D1})}{R^2_{DA}} - \frac{1}{2}\frac{(\vec{r}_{A2} - \vec{r}_{D1})^2}{R^2_{DA}} + \frac{3}{2}\left(\frac{\vec{R}_{DA} \cdot (\vec{r}_{A2} - \vec{r}_{D1})}{R^2_{DA}}\right)^2 + \cdots\right] \tag{4.35}$$

It is easily remarked that only the cross terms of $r_{A2}$ and $r_{D1}$ contribute to the $V_{DA}$, because of the orthogonality for quantum state. Note that the transition electrical dipoles for donor and acceptor are:

$$\vec{\mu}_D = \sqrt{2}\langle \psi_{D^*} | e\vec{r}_{D1} | \psi_D \rangle$$
$$\vec{\mu}_A = \sqrt{2}\langle \psi_{A^*} | e\vec{r}_{A2} | \psi_A \rangle$$

Then $V_{DA}$ can be simplified as:

$$V_{DA} = \frac{\vec{\mu}_A \cdot \vec{\mu}_D}{R^3_{DA}} - \frac{3(\vec{R}_{DA} \cdot \vec{\mu}_A)(\vec{R}_{DA} \cdot \vec{\mu}_D)}{R^5_{DA}} \tag{4.36}$$

That is, the coupling arises from the coupling between donor and acceptor through transition electrical dipole interaction: an electronic excited state is viewed as fluctuating electrical dipole, or electron-hole pair formed by promoting electron from occupied MOs to unoccupied MOs. This approach averages away the shapes of the donor and acceptor molecules and should be applied when the size of the interacting molecules is small with respect to the intermolecular separation [67].

A more general expression can be obtained through transition density distribution. In fact, the transition dipole can be rewritten as:

$$\vec{\mu}_D = \int d\vec{r}\rho_D^{ge}(\vec{r})e\vec{r} \tag{4.37}$$

Here:

$$\rho_D^{ge}(\vec{r}) = N \int \cdots \int \mathrm{d}\vec{\mathbf{r}}_2 \ldots \mathrm{d}\vec{\mathbf{r}}_N \Psi_g(\vec{\mathbf{r}}, \vec{\mathbf{r}}_2, \ldots, \vec{\mathbf{r}}_N)\Psi_e^*(\vec{\mathbf{r}}, \vec{\mathbf{r}}_2, \ldots, \vec{\mathbf{r}}_N)$$

The intermolecular excitation coupling can be now rewritten as:

$$V_{DA} = \mathrm{e}^2 \sum_{\sigma}^{D} \sum_{\tau}^{A} \frac{\rho_D(\sigma)\rho_A(\tau)}{r_{\sigma\tau}} \tag{4.38}$$

Here $r_{\sigma\tau}$ represents the distance between atomic centers $\sigma$ and $\tau$, and $\rho_D(\sigma)[\rho_A(\tau)]$ is the atomic transition density on site $\sigma$ [$\tau$]. This expansion for the Coulombic interaction is beyond the dipole-dipole level and has been applied for several conjugated systems [68–71]. When the separation of D and A is comparable to their physical sizes, the topology of the transition densities cannot be ignored [72].

The transition density cube (TDC) method has been developed to calculate the coupling according to (4.38), of which the donor and acceptor transition densities are each represented in a 3D grid [68, 73]. Nevertheless, this approach requires a large amount of computer time and the numerical quality is rather limited due to the steep cusp in the Coulomb kernel $1/r_{12}$. Hsu et al. [73, 74] have embedded the Coulomb coupling calculation by analytically solving (4.30). Moreover, they developed the fragment excitation difference (FED) method to calculate the excitation energy transfer coupling which includes the Coulomb interaction, exchange interaction as well as a term arising from the overlap of donor-acceptor electronic densities. Their results showed that, for a pair of stacked naphthalenes, the Coulombic interaction dominates the electronic coupling after 5 Å face-to-face separation [74].

We tested the Coulomb coupling calculation for such a pair of stacked naphthalenes. Only the Coulombic interaction between the ground state and lowest excited state ($L_a$ or $1^1B_{2u}$) is presented here based on CIS/3-21G. According to Förster mechanism, the acceptor molecule is optimized in its ground state, while the donor molecule is optimized in its lowest excited state, both at the B3LYP/6-31 g* level. From Fig. 4.5, our calculation is in nice agreement with [73]. It is found that the Coulomb coupling decays as $d^{-3}$ for the stacked naphthalenes.

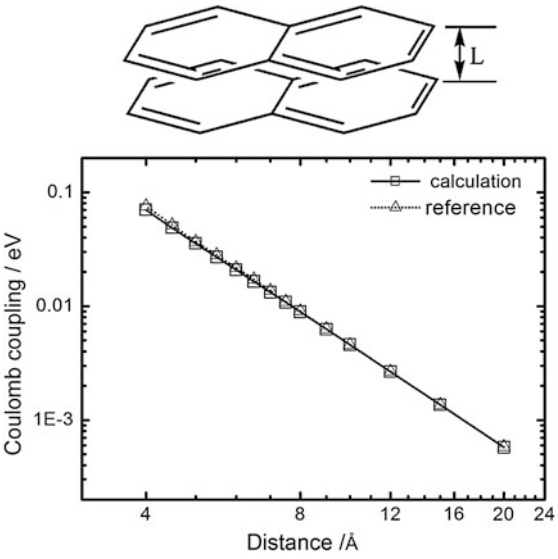


**Fig. 4.5** Coulomb coupling as a function of intermolecular separation for a pair of naphthalene for the $L_a$ ($1^1B_{2u}$) state between a pair of stacked naphthalenes

## 4.4 Dynamic Monte Carlo Simulation of Bulk Heterojunction Device

Theoretical progresses have been made towards quantitative predictions of opto-electronic properties for organic electronics, such charge mobility in organic field-effective transistors [36–39] and light-emitting efficiency and optical spectrum [42]. However, for the photovoltaic performance, theoretical treatments at present stage are quite fragmented, namely, we have good knowledge for the donor-acceptor interfaces [24–26], or optical absorption and emission as demonstrated in Sect. 4.2 of this chapter, or the exciton diffusion processes. However, we still do not get a unified approach to predict the power conversion efficiency starting from first-principles. We describe here a continuum device model which assumed uniformly distributed p-n junction in the bulk materials [75] and the dynamic Monte Carlo (DMC) approach developed to simulate complicated chemical processes, proposed first by Watkins et al. [76]. The basic algorithm of DMC is based on first-reaction method (FRM) [77] to describe the key processes, the exciton generation, diffusion, the dissociation at the interface, the charge drift and diffusion and the injection from the electrodes, and the collection by the electrodes [78]. Previous simulations have always assumed balanced electron and hole transports, namely, equal charge mobility, in order to avoid space charge accumulation. Such simplification has been removed recently by Yang and Forrest [79] and Meng et al. [80], by combining DMC with a Poisson equation solver, which can present the electrostatic potential according to the charge density, and in turn, the potential influence both the charge and exciton transport.

The first step is to generate morphology for the polymer donor and fullerene acceptor blends. The easiest way for describing the two-phase structure is to use Ising model. In the Ising model, the spin up and down correspond to the donor and acceptor phases, respectively [76], and the Hamiltonian for the energy contributed to site $i$ is:

$$\varepsilon_i = -\frac{J}{2}\sum_j (\delta_{s_i,s_j} - 1) \tag{4.39}$$

where $\delta_{si,sj}$ is the Dirac delta function, and $s_i$, $s_j$ are the spin indices at site $i$ and $j$. The summation over $j$ includes all first and second nearest neighbors, and the energetic interaction is inversely proportional to the distance between neighboring sites $i$ and $j$ (the energy is scaled by a factor of $1/\sqrt{2}$ for the second nearest neighbors). To obtain a series of morphologies with different phase interpenetration, we need to decide the appropriate initial configuration and the corresponding interaction energy $J$. In our simulation, the initial morphology with minimal phase separation is chosen and the interaction energy $J$ is set as +1.0 $k_B T$. To relax the system to an energetically stable state, the neighboring pairs of sites are chosen randomly in system, and then the acceptance probability for an attempt to swap the site spins is calculated as:

$$P(\Delta\varepsilon) = \frac{\exp(-\Delta\varepsilon/(k_B T))}{1 + \exp(-\Delta\varepsilon/(k_B T))} \tag{4.40}$$

where Δε is the total energy change caused by swapping the site spins. After a large number of attempted spin swapping, a desired morphology series with varying scale of phase separation can be generated and stored for later use.

Two special cases: the bilayer morphology (M1 in Fig. 4.6) and an optimal checkered structure (M4 in Fig. 4.7) are also chosen in the simulation for comparison, in addition to the well dispersed morphology M3 and the less separated M2.

In the model system, the lattice is of the 60 × 60 × 30 sites in the $x$, $y$, and $z$ directions, respectively, and a lattice constant of 3 nm is used. A single occupancy of lattices for any particle (exciton, electron or hole) is imposed, and the system temperature $T$ is fixed at 298 K. The electrodes are in the $x$-$y$ plane located at $z = 0$ and $z = 90$ nm. Periodic boundary conditions are applied in both $x$ and $y$ directions. We note that the thickness of solar cell active layer is around 100 nm.

Three types of mobile particles (electrons, holes and excitons) are considered in our simulation. In the first reaction method (FRM), [77, 81, 82, 83], the description for each of the particle is associated with an event, and each event has a waiting time $\tau_q$. An event is associated with a configurational change in system, e.g., inserting or removing a particle, updating the coordinates of particles. All the possible events in the system are stored in an ascending order for waiting time and form a temporal sequence. This queue of events will constantly be updated to reflect the time evolution

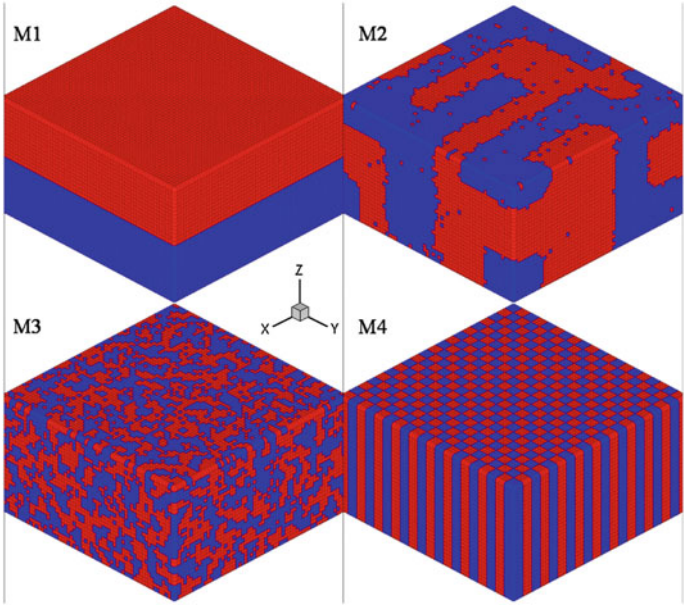


**Fig. 4.6** Typical morphologies with different scale of phase separation, *M1* for the bilayer, *M2* and *M3* for the blend generated by using the Ising Model, and *M4* for the checkered structure. The electron and hole conductors are colored with *red* and *blue*, respectively

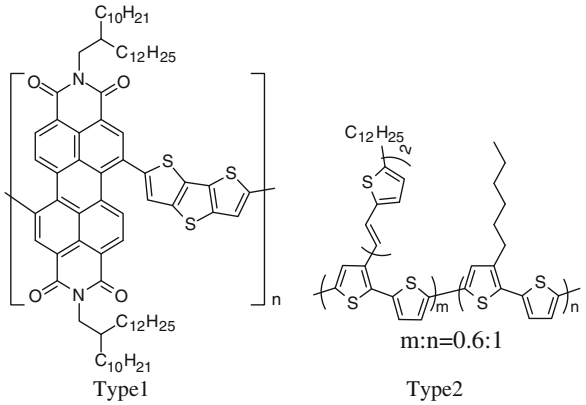


**Fig. 4.7** The chemical structures of poly(perylene diimide-*alt*-dithienothiophene) (PPDI, *Type 1*) and bis (thienylenevinylene)-substituted polythiophene (PBTT, *Type 2*)

of the system. At each time step, the event at the start of the queue is selected to execute and then removed from the queue. Later on, the simulation time is incremented by the time expired and all of the waiting times in queue are reduced by this time expired. The execution of a current event will probably preclude the occurrence of subsequent events in conformance with certain rules, e.g., the single occupancy of lattices, and in turn it requires that the newly enabled event be created and then

inserted in the queue. Marsh et al. [83] have demonstrated that the dynamic properties of carriers can be indistinguishably described by both the FRM and the full dynamical Monte Carlo algorithm (in which the whole event queue must be updated for every configuration change).

The waiting time $\tau_q$ is calculated as:

$$\tau_q = -\frac{1}{W}\ln(X) \tag{4.41}$$

where $X$ is a random number uniformly distributed in (0, 1), and $W$ is the occurring rate of an event. Only the event occurring first is inserted in the queue. As a result, we need to calculate the waiting time for all the events and select the event with the shortest waiting time. Then this time increment is counted in the simulation.

The model system we choose is a polymer blend of PPDI [84] and PBTT [85], see Fig. 4.7. The fabricated all-polymer solar cell exhibited strong absorption throughout the visible and extending into the near infrared range. The charge mobilities are also relatively high with electron mobility for PPDI about $1.3 \times 10^{-2}$ and hole mobility for PBTT $\sim 10^{-3}$ $cm^2/Vs$. The power conversion efficiency is found to be greater than 1 % at the beginning, and later, was increased to 1.5 %. The purpose of this study is to find out the essential processes determining the photovoltaic effect, in order to achieve the optimal performance.

The donor and acceptor polymers are simplified in a lattice model, distributed in the morphology generated in Fig. 4.6. Excitons are created at randomly chosen sites in either the hole or electron polymer at constant rate. From the experimental absorption spectrum, the exciton generation rate is calculated to be 900 $s^{-1}$ $nm^{-2}$ at AM1.5 with illumination of 90 $mW/cm^2$ by integrating of the spectrum up to 800 nm. Note that one can convert the solar emission spectrum to obtain a photon irradiation rate at 4,000 $s^{-1}$ $nm^{-2}$. Namely, the quantum efficiency upper limit is 900/4,000 = 22.5 % for such blend. Right after the exciton creation, there are three events followed: hopping, recombination and dissociation at the interface, before charge collection at the electrodes. The excitons generated in these polymers are assumed to be singlet prior to dissociation at the donor and acceptor interface. Therefore, the exciton dissociation rate $W_{ed}$ must be set sufficiently high, namely, in the simulation, once we find the exciton reaches interface, the dissociation event is put on the top priority.

In organic semiconductors, the exciton lifetime ranges from a few hundreds picoseconds to a few nanoseconds. The diffusion length of exciton is estimated to be around 10–20 nm in these polymers. The exciton hopping follows a Förster process, namely, the hopping rate from site $i$ to a nearby site $j$ is given by

$$W_{ij} = W_e\left(\frac{R_0}{R_{ij}}\right)^6 \tag{4.42}$$

where $R_{ij}$ is the distance between sites $i$ and $j$, $R_0$ is the exciton localization radius, and $W_e$ is the hopping attempt frequency. Hopping rates for excitons are evaluated

by including lattice neighbors out to a radius of 15 nm. The parameters $W_e R_0^6 = 2\ \mathrm{nm}^6\ \mathrm{ps}^{-1}$ and exciton recombination rate $W_{er} = 1/500\ \mathrm{ps}^{-1}$ are set, so that the exciton diffusion length is around 10 nm. In our model, the exciton hopping is only allowed between the same type of site.

Charge carriers (electrons and holes) are generated either from the exciton dissociation or injection from the electrodes, and the electron (hole) can only occupy the acceptor (donor) site. All electrostatic interactions in the device are included in the model, and the Coulombic interaction between sites $i$ and $j$ is calculated as:

$$V_{ij} = \frac{q_i q_j}{4\pi\varepsilon_0 \varepsilon} \frac{1}{R_{ij}} \tag{4.43}$$

where $q_i$ and $q_j$ are the site charges respectively, $\varepsilon$ is the dielectric constant and $R_{ij}$ is the distance between sites $i$ and $j$.

The created charge carrier moves following Marcus theory [86] to hop in the bulk:

$$W_{ij} = V_{hop} \exp\left(-\frac{(E_j - E_i + E_r)^2}{4E_r k_B T}\right) \tag{4.44}$$

$E_i$ and $E_j$ are the energies of hopping sites $i$ and $j$, containing the internal electric field effect solved from Poisson equation, and $E_r$ corresponds to charge reorganization energy. For the charge carriers, all the Coulomb interactions between neighboring charges (within a distance less than $R_c$) and modifications from the effect of the internal electric field (Poisson equation solution) are included in calculating the site energy. Hopping is restricted to the adjacent sites (the nearest neighboring sites, thus there are 6 adjacent sites in a cubic lattice), whose energy is calculated by taking into account of the Gaussian standard deviation $\sigma$ to the density of states. The prefactor $V_{hop}$ is derived from the Einstein relationship under isoenergetic site condition as:

$$V_{hop} = \frac{6 k_B T \mu_{e/h}}{q a_0^2} \exp\left(\frac{E_r}{4 k_B T}\right) \tag{4.45}$$

where $\mu_{e/h}$ is the electron/hole mobility. If the electron and hole are located on the adjacent sites, they may recombine with a rate $W_{cr}$. A charge carrier adjacent to the electrode is extracted from the device with a rate $W_{ce}$, which is calculated by using the Marcus formula. The energy difference (driving force) between the Fermi level of an Al electrode and the LUMO of PPDI is taken as $-E_{IB} = -0.4$ eV. We will treat this extraction as an inverse process of charge injection and then $W_{ce}$ is calculated. To simulate the effect of "charge leak", the electron (hole) can be extracted from the device at both the cathode and anode. The image charge effects are also included in calculating the Coulombic interactions for charges near the electrodes (up to the cutoff radius) [87–89]. The charge attraction barrier $U$ actually depends as well on

the external electric field and the Coulomb field binding the carrier with its image twin in the electrode [88, 89]:

$$U = E_{IB} - \frac{q^2}{16\pi\varepsilon_0\varepsilon a_0} - qFa_0 \tag{4.46}$$

where $a_0$ is the lattice constant, $E_{\mathrm{IB}}$ the barrier height in the absence of both electric field and image charge effect, $F$ the electric field solved from Poisson equation, $q$ the elementary charge, $\varepsilon$ the medium dielectric constant, and $\varepsilon_0$ the electric permittivity.

The charge injection is restricted to the lattice sites in contact with an electrode, that is, the electron conductor lattice near the cathode and the hole conductor lattice near the anode; thus, the distance of the injection contact is fixed to the lattice constant in (4.45). The subsequent charge carrier motions in the device will take fully account of the local electric field. Near the electrodes, the image charge effects are included up to a cutoff distance of 15 nm.

The conventional Miller-Abrahams expression has been used to calculate the rate of a charge jumping from the Fermi level of the electrode to a site in the dielectric [87]; by considering the restriction on the injection sites, the Miller-Abrahams expression is simplified as:

$$W_{ij} = W_0 \begin{cases} \exp\left(-\frac{E_j - E_i}{k_B T}\right) & : \quad E_i < E_j \\ 1 & : \quad E_i \geq E_j \end{cases} \tag{4.47}$$

where the prefactor $W_0$ is derived from the Einstein relation under isoenergetic site condition as:

$$W_0 = \frac{6k_B T\,\mu_{e/h}}{qa_0^2} \tag{4.48}$$

The Gaussian standard deviation $\sigma$ to the density of states is taken into account in the calculation of the site energies for charge injection. Therefore, the site energies are taken as $E_j = U + \sigma R$ and $E_i = \sigma R$, where $R$ is a normally distributed random number and $U$ is calculated by using (4.46).

The freshly generated charge carriers are not allowed to be extracted instantly. To be specific, any charge carrier created adjacent to the electrodes must hop at least one step in the polymer blend before it can be extracted. These different treatments for charge injection and charge extraction can lead to appropriate charge densities adjacent to the electrodes, which enable us to numerically solve the Poisson equation.

For a conventional inorganic solar cell, thermally-activated charges represent another source of dark current in addition to charge injection. Therefore, exciton thermal activation is also incorporated into our FRM algorithm to simulate the dark saturation current density $J_{\mathrm{S}}$ under reverse bias voltage. Thermally activated

excitons undergo exciton diffusion and charge separation at the interface in the same way as photo-generated excitons. The generation rate for the thermally activated excitons is evaluated based on the dark saturation current density $J_S$ under reverse bias voltage. In practice, the thermal generation rate $W_{egt} = 32\ s^{-1}\ nm^{-2}$ is set for thermally activated excitons, which leads to a dark current density $J_S \approx 0.36\ mA/cm^2$ under the external applied voltage of −1.5 V. This simulation result is consistent with the experimental dark saturation current density of $0.37\ mA/cm^2$ [84].

The coupled Poisson equation in the dynamic Monte-Carlo is:

$$\frac{\partial^2}{\partial z^2}\psi(z) = \frac{q}{\varepsilon_0 \varepsilon}[n(z) - p(z)] \tag{4.49}$$

This equation relates the potential $\psi$(z) to the electron and hole densities $n$(z) and $p$(z) in the system. The Gummel iteration method is utilized to solve the discretized Poisson equation [90]. To simulate the device performance under dark condition for the polymer blend, the boundary condition for the potential in solving the Poisson equation can be set as:

$$\psi(L_z) - \psi(0) = V_a \tag{4.50}$$

where $V_a$ is the external applied voltage and $L_z$ is the device dimension in the $z$ direction. This is based on the assumption that an organic photovoltaic device in the dark is in equilibrium in the case of zero external field ($V_a = 0$), which is similar to the situation in a traditional inorganic device.

Under illumination, the open-circuit voltage $V_{OC}$ is determined by a number of possible factors: the light-induced splitting of the quasi-Fermi levels, which is related to the difference between the electron affinity (or crudely speaking the LUMO level) of the acceptor material and the ionization potential (HOMO level) of the donor material in the active layer. Therefore, the boundary condition for the potential in solving the Poisson equation under illumination is set as [91]:

$$\psi(L_z) - \psi(0) = V_a - \frac{1}{q}E_{gap} \tag{4.51}$$

where $E_{gap}$ is the energy difference between the electron affinity of the acceptor material and the ionization potential of the donor material.

The solution to the Poisson equation with the boundary condition gives the total electrostatic potential due to space charge and a linearly distributed driving potential. It can be derived that the driving electric field is simply the average of the total electric field at the boundaries. In the DMC simulation, the charge drift is governed by the Coulombic interactions and the driving electric field obtained by solving the Poisson equation. The driving force due to the difference in the work functions between the electrodes is no longer considered. Thus all electrostatic or Coulombic interactions in the device have been included in the DMC-PE model.

By considering charge injection and thermal activation, the charge accumulation process in the device is enhanced. The charge recombination rate is thus set at $10^{-5}$ $ps^{-1}$ to balance the excess charge density. These values lead to a typical charge density of $\sim 10^{22}$ $m^{-3}$ when the charge mobilities are set either to the same equal values as in the previous DMC simulations (e.g., $\mu_n = \mu_p = 10^{-3}$ $cm^2$ $V^{-1}$ $s^{-1}$) [78] or to different values as measured experimentally (e.g., $\mu_n = 10^{-2}$ $cm^2$ $V^{-1}$ $s^{-1}$ and $\mu_p = 10^{-4}$ $cm^2$ $V^{-1}$ $s^{-1}$) for the polymer blend [84].

Thus, we now sketch the combined dynamic Monte Carlo simulation and Poisson equation method in Fig. 4.8, while all the parameters are listed in Table 4.4.

The simulation is required to reach a steady state, and the internal quantum efficiency (IQE) and the current density for different conditions are saved and calculated over a time interval long enough to average out the fluctuations (typically >0.1 s). Under the current assumption, the parameters will not change with the scale of phase separation. The charge extracted from the electrodes per area and unit time is taken as the current density. Then, the outside circle current is calculated as the average of the net current density at the cathode and anode respectively.

Under the short-circuit conditions, the IQE and its two constituent components, exciton dissociation efficiency (the ratio of the number of excitons dissociated to the number of excitons generated) and charge collection efficiency (the ratio of the net number of charges that exit the device to twice of the number of excitons dissociated), are calculated for various blends and checkered morphologies, and are plotted as shown in Fig. 4.9. Generally, the exciton dissociation tends to increase, while the charge collection efficiency will decrease as the interfacial area increases.

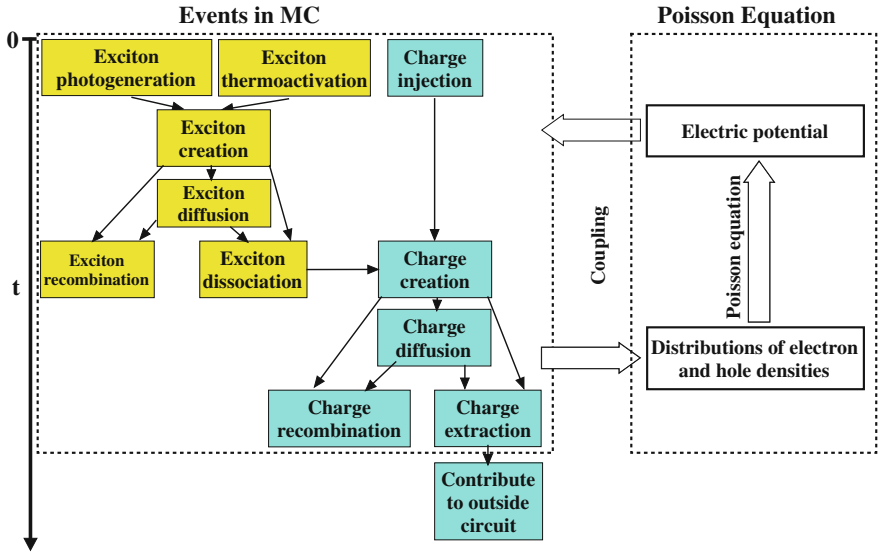


**Fig. 4.8** Schematic representation of the dynamic Monte Carlo coupled to the Poisson equation (DMC-PE) simulation processes

**Table 4.4** Parameters used in the DMC-PE modeling

| | | |
|---|---|---|
| T | 298.0 K | Temperature |
| ε | 3.5 | Dielectric constant |
| $a_0$ | 3 nm | Lattice constant |
| $R_c$ | 15 nm | Cutoff distance |
| $W_{eg}$ | 900 $s^{-1}$ $nm^{-2}$ | Exciton creation rate for photo-generated excitons |
| $W_{egt}$ | 32 $s^{-1}$ $nm^{-2}$ | Exciton creation rate for thermo-activated excitons |
| $W_eR_0^6$ | 2 $nm^6$ $ps^{-1}$ | Exciton hopping rate |
| $W_{er}$ | $2 \times 10^{-3}$ $ps^{-1}$ | Exciton recombination rate |
| $E_r^*$ | 0.187 eV | polaron binding energy |
| $V_{hop}$ (p) | $1.06 \times 10^{-3}$ $ps^{-1}$ | Charge hopping rate prefactor for holes |
| $V_{hop}$ (n) | $1.06 \times 10^{-1}$ $ps^{-1}$ | Charge hopping rate prefactor for electrons |
| $\sigma^*$ | 0.062 eV | Gaussian standard deviation |
| $W_{cr}$ | $1 \times 10^{-5}$ $ps^{-1}$ | Charge recombination rate |
| $E_{IB}$ | 0.4 eV | Difference between LUMO (A) and Fermi level of aluminum cathode |
| $E_{gap}$ | 1.1 eV | Difference between LUMO (A) and HOMO (D) |
| $J_S$ | 0.36 $mA/cm^2$ | Dark saturation current density |

The parameters marked with an asterisk are taken from [83]

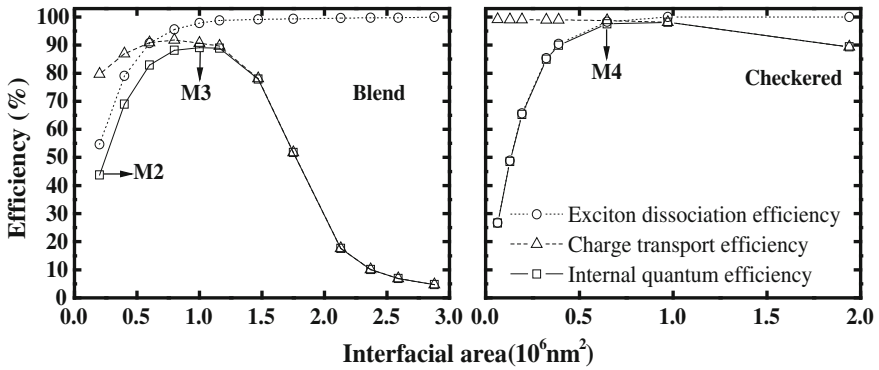


**Fig. 4.9** For the blend and checkered morphologies, the exciton dissociation efficiency, the charge collection efficiency, and the internal quantum efficiency vary with interfacial area between the electron and the hole conductors

These lead to the peak of IQE, corresponding to the characteristic feature size of around 10 nm, while for the checked series, the maximum IQE occurs when the width of the square rods is around 9 nm. For the blend morphologies with low interfacial area, e.g., the M2, the pure phases are not perfectly separated due to the thermal effect in the Ising model, and thus many small isolated islands remain in

those majority phases. These islands tend to act as traps for the free charges which can only be got rid of by waiting for the opposite charges to recombine at the interface between the islands and the majority phases. As a result, the charge collection efficiency for the M2 cannot reach the 100 % level as expected, while a peak can occur at a large-scale phase separation.

The calculated *I–V* curves under both dark and illumination conditions are shown in Fig. 4.10. It can be seen that our simulation results provide a consistent picture of the device performance under dark condition. Similar to the photo-generated current, the dark current is also sensitive to the morphology of the polymer blend. Note that an optimized morphology structure (peak in Fig. 4.9) is used in the calculation. That explains both the photo- and dark currents are larger than the experimentally measured values. The experimental mobilities ($\mu_n = 10^{-2}$ cm$^2$ V$^{-1}$ s$^{-1}$, $\mu_p = 10^{-4}$ cm$^2$ V$^{-1}$ s$^{-1}$) are used in the simulation.

For an ideal solar cell, it is assumed that the photogenerated current density $J_{ph}$ is voltage independent, which means that $J_{ph}$ is equal to the short-circuit current density $J_{SC}$ at any applied voltage [92, 93]. The simulated open-circuit voltage, 0.64 V, is in excellent agreement with the experimental data (0.63 V) [84], as shown in Fig. 4.10. Under the open-circuit condition, the dark current from injection has strongly increased and eventually cancels the photogenerated current. More precisely, two types of current present, driven by different effective voltages that cancel each other: one from injection with the open-circuit voltage as the effective voltage, while the other from exciton dissociation for which the effective drive voltage is the open-circuit voltage shifted by the energy difference between the acceptor and donor materials $E_{gap}$ (4.51).

Such agreement convinces us that the DMC-PE model can provide reasonable description for the performance of organic solar cells. Since the open-circuit voltage is due to the cancellation of the photo-generated current and the dark current, it requires that any approach increasing the photo-generated current with respect to the injected current can enhance the open-circuit voltage. For example, it has been

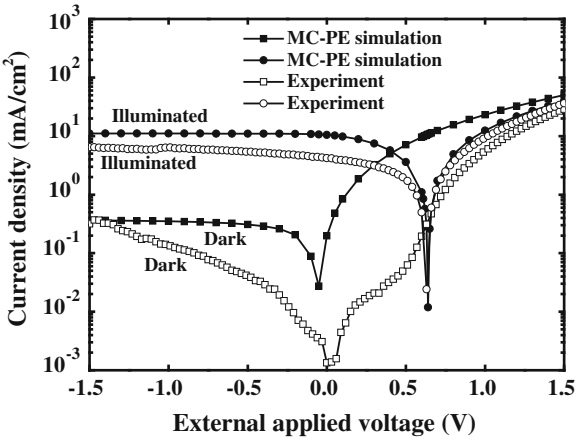


**Fig. 4.10** Comparison of the *I–V* curves from the DMC-PE simulations and experiments

found that increasing the exciton dissociation rate [94], which increase the photo-generated current, becoming beneficial to the enhancement of the open-circuit voltage.

By incorporating the Poisson equation into the DMC model with FRM, the constraint of having to consider balanced mobilities for electrons and holes in the polymer blend is removed. Some of the key physical properties we are interested in, e.g., the potential and charge density distributions, can now be studied more appropriately. As shown in Fig. 4.11, when electrons and holes have equal mobilities, the potential distribution in the OPV device is nearly linear; this confirms our previous assumption that, in a polymer blend with balanced carrier mobilities [78, 95] the charge drift is determined by a linear electric field. When mobilities for electrons and holes are different, which is usually the case and here $\mu_n > \mu_p$ for the polymer blend, the potential distribution becomes more complicated and space charges begin to accumulate in the device. As a consequence, the electric field increases in the region near the anode to enhance the extraction of holes, as shown in Fig. 4.12, while in the region near the cathode the electric field decreases to suppress the extraction of electrons. As the difference in the mobilities of hole and electron increases, deviation from linearity for the potential distribution in the polymer blend is remarkable.

We also investigate the effects of exciton creation rate, charge mobility, and charge recombination rate on the short-circuit current and the IQE. As shown in Fig. 4.12, the short-circuit current increases sublinearly with increasing light intensity or exciton creation rate. However, when the charge mobility is over $10^{-3}$ $cm^2$ $V^{-1}$ $s^{-1}$, the short-circuit current and the internal quantum efficiency become less sensitive to the mobility. As a result, further increase in mobility does not significantly improve the device performance. This means that as a way to

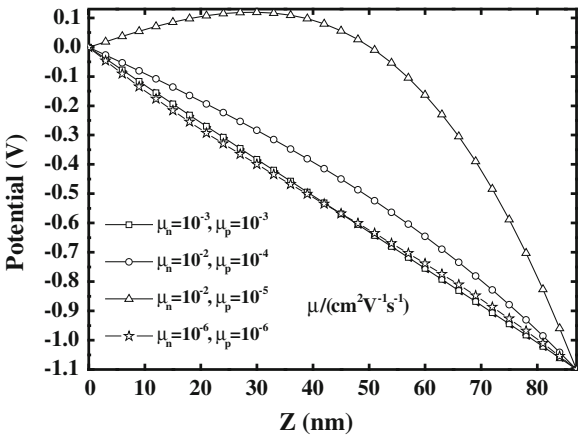


**Fig. 4.11** The electrostatic potential distribution in the device under short-circuit condition. As the difference in hole and electron mobilities increases, the space charge accumulation effects are enhanced, which cause the potential to gradually deviate from the linear distribution

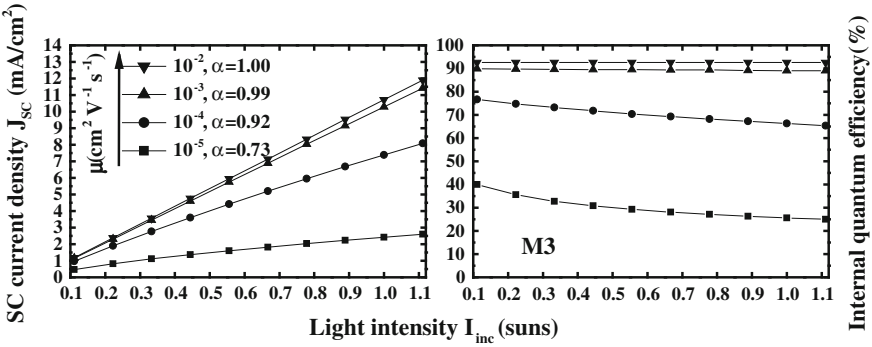


**Fig. 4.12** The dependency of short-circuit current and internal quantum efficiency on the mobility and the light intensity for the morphology M3. $J_{SC}$ is related to $I_{inc}$ as $J_{SC} \propto I_{inc}^{\alpha}$, and $\alpha$ varies with mobility

improve the PCE, the strong absorption is more effective than the high mobility, especially as the particular mobility is high enough to extract almost all the charges diffusing in the system.

A typical feature of organic solar cells is that the short-circuit current density $J_{SC}$ does not scale linearly with the exciton generation rate $W_{eg}$ or light intensity $I_{inc}$ [87]. Instead, a power law relationship is found and given by $J_{SC} \propto I_{inc}^{\alpha}$, where $\alpha \leq 1$ [88, 91]. Such deviation from linearity has been ascribed to nongeminate charge recombination [76, 91]. When the charge mobility decreases, the average time for free charges exiting from the device tends to increase, and the occurrence probability of nongeminate charge recombination would increase. This results in a bigger deviation from unity for $\alpha$, and more rapid decrease in IQE with increasing light intensity, as shown in Fig. 4.12.

Recent theoretical calculations based on analysis of energy levels of frontier orbits have predicted that 15 % power conversion efficiency for polymer/fullerene system is possible [96]. For the fill factor 0.65, we simulate PCE contour curves as a function of the blend morphologies and the charge mobility as plotted in Fig. 4.13. It should be noted that the optimal 5 % PCE is limited by many factors listed in Table 4.4. Figure 4.13 shows that by improving the polymer morphology and increasing the charge mobility, the PCE can be increased from the experimental value of 1.3 % to about 5 %.

## 4.5 Continuum Device Model

The continuum device model, or drift-diffusion model, captures the drift of carriers under an electric field and diffusion due to the gradient in concentrations [97]. In modeling the electronic process in organic light emitting diodes (OLEDs), such approach has been widely employed [98, 99], and recently, it has been extensively

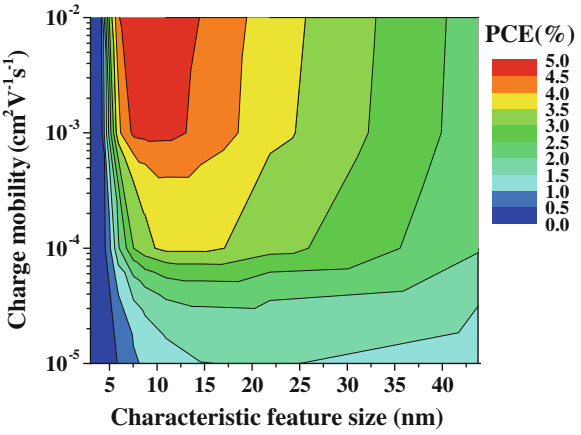


**Fig. 4.13** Contour plots showing the calculated power conversion efficiency (PCE) for the blend morphologies versus the charge mobility and the characteristic feature size in the blend

applied in modeling photovoltaic devices [75, 100–108]. Barker et al. [100] developed a one-dimensional device model for a bilayer organic device. The experimental data can be well reproduced. In their approach, electrons and holes are assumed to be only generated directly by absorbing a fraction of incident light leading to charge separation at interface. Koster et al. [75] has demonstrated an equilibrium one-dimensional device model for the BHJ solar cells. The model includes drift and diffusion of charge carriers, the influence of space charge on the electric field, field- and temperature-dependent generation of free charge carriers, and bimolecular recombination. The current density-voltage (J-V) characteristics are solved self-consistently which are shown to be in excellent agreement with the experimental curves. Here, we are reviewing some of the recent progresses in drift-diffusion model and will apply it to model the low band gap polymer solar cell.

The solar emission generates exciton in polymer and the exciton migrates to the donor acceptor interface to generate bound electron and hole pair. The bound e-h pair may dissociate into free carriers with a rate $k_d$ or geminately decay to the ground state with a rate $k_f$. The separation of e-h pair is a competition between dissociation and decay. According to Braun's model [109], the probability of e-h pair dissociation is given by

$$P = k_d / (k_d + k_f) \tag{4.52}$$

Once the e-h pair is dissociated, the free charge carriers have to move toward the respective electrodes, generating steady current in the device. The electron (hole) current density $J_{n(p)}$ has two contributions: the drift current due to the electrostatic potential gradient and the diffusion current due to the charge density gradient as determined by the following equations:

$$J_n = -qn\mu_n \frac{\partial}{\partial x}\psi + qD_n \frac{\partial}{\partial x}n \quad \text{and} \quad J_p = -qp\mu_p \frac{\partial}{\partial x}\psi - qD_p \frac{\partial}{\partial x}p, \tag{4.53}$$

where $q$ is the elementary charge, $D_{n(p)} = \mu_{n(p)} k_B T/q$ is the carrier diffusion coefficient [97] and $\mu_{n(p)}$ is the carrier mobility. The electrostatic potential $\psi$ and the electron (hole) density $n(p)$ satisfy the Poisson equation

$$\frac{\partial^2}{\partial x^2}\psi(x) = \frac{q}{\varepsilon}[n(x) - p(x)], \tag{4.54}$$

where $\varepsilon$ is the dielectric constant. When electrons and holes meet during transport, there occurs charge recombination. The bimolecular recombination is one of the most important charge-carrier loss mechanisms. And for some system, the loss is mainly through charge traps. The bimolecular recombination rate is

$$R = k_r(np - n_{int}^2) \tag{4.55}$$

where the bimolecular recombination constant is $k_r = \frac{q}{\varepsilon}\min(\mu_n, \mu_p)$, and $n_{\text{int}} = N_c \exp(-qE_{gap}/k_B T)$ is the intrinsic carrier density of electrons/holes, where $N_c$ is the effective density of states of either conduction or valence band edge.

The net generation of free charge carriers depends on e-h pair generation and its subsequent dissociation as well as recombination. In steady-state, the number of bound e-h pairs per unit volume (X) follows:

$$\frac{dX}{dt} = G - k_f X - k_d X + R = 0 \tag{4.56}$$

where G is the generation rate of e-h bound pair. The net generation rate of free charge carriers $U$ is then written as

$$U = k_d X - R = PG - (1 - P)R \tag{4.57}$$

Here, $U$ is related to the gradient of current density $J_{n(p)}$ through the continuity equations

$$\frac{\partial}{\partial x}J_n(x) = qU(x) \quad \text{and} \quad \frac{\partial}{\partial x}J_p(x) = -qU(x) \tag{4.58}$$

To obtain a solution of the equations, boundary conditions of charge densities and electrostatic potential are essential. The effective electron and hole densities at respective electrode equal to $N_c$ gives the boundary condition for carrier densities. And (4.50) serves as the boundary condition for the electrostatic potential. Poisson equation and the continuity equations could be solved iteratively by a numerical scheme developed by Gummel [90]. Finally, the J-V curve and carrier densities can be obtained.

The separation of bound e-h pairs into free charges is an important process in BHJ solar cells. The photocurrent is governed by the field and temperature dependent dissociation of e-h pairs according to Onsager's theory [110]. Braun has made an important refinement to this theory by pointing out that the bound e-h pair has a finite lifetime [109]. Therefore, the exciton dissociate rate $k_d$ can be calculated according to

$$k_d = \frac{3R}{4\pi a^3} e^{-E_b/kT}(1 + b + \frac{b^2}{3} + \cdots) \tag{4.59}$$

where $R$ is the Langevin bimolecular recombination rate, $E_b$ is the e-h pair binding energy $\sim q^2/(4\pi\varepsilon a)$, and $b = q^3F/(8\pi\varepsilon k_B^2T^2)$, $F$ is the electric field strength. Recently, an extended Onsager theory has been proposed based on finite recombination rate at nonzero reaction radius [111]. It was found that the exponential kinetics for both recombination and separation processes assumed in Braun's model might not be true.

Several models have been proposed to describe the charge recombination mechanism. These include: (i) the original and classical Langevin model [112] with the recombination rate constant $k_r = \frac{q}{\varepsilon}(\mu_n + \mu_p)$; (ii) the minimum mobility model [113] where the recombination rate constant is given by $k_r = \frac{q}{\varepsilon}\min(\mu_n, \mu_p)$; (iii) the potential fluctuation model [114] where a potential barrier was imposed, $k_r = \frac{q}{\varepsilon}\exp(-\frac{\Delta E}{k_BT})(\mu_n + \mu_p)$; (iv) carrier concentration gradient model [115] in which the recombination rate is proportional to the local product of electron and hole concentrations; (v) two-dimensional Langevin recombination theory [116] where the recombination rate depends on the square root of density of charge carriers; and (vi) unified theory of geminate and bulk electron-hole recombination [117] where the recombination occurring at a nonzero separation with a finite intrinsic rate is taken into account to explain the observed much smaller recombination rate constant than those predicted from Langevin theory.

Since the one-dimensional drift-diffusion model can only be applied to BHJ or bilayer system can only describe motion in one-dimension across the active layer, ignoring the 3-D morphology effect. A natural extension of the current model to higher dimension is expected to be able to account for the effect of morphology. Buxton and Clarke [101] developed a two-dimensional device model to simulate the morphological effects such as domain size, order and percolation on J-V curve and other device performance. However, the dissociation probability of e-h pairs is not properly taken into account. Williams and Walker [118] presented a two-dimensional model in which the effects of optical interference and the competition between dissociation and decay of e-h pairs were considered. Maturova et al. [103, 104, 106] also developed a two-dimensional morphological model, where the active layer is divided into two regions, called donor–acceptor mix and acceptor pure phases. Since the precise location of charge separation could not be specified, to establish the quantitative relationship between the performance of solar cells and the degrees of phase separation remains a challenging issue.

On the other hand, such equilibrium device model can only give a description of the steady-state behavior. Hwang and Greenham [102] utilized a time-dependent device model to deal with the transient photocurrent of organic BHJ solar cells. The simulated transient photocurrent reproduced the experimental results. They further improved the time-dependent device model by incorporating electron trapping [105].

Now, we are ready to apply the above mentioned methods to model the BHJ solar cell, namely, to simulate J-V curve. The primary objective is to establish quantitative relationship between the device performance and the microscopic processes such as charge dissociation and recombination rates, and charge mobility.

Recently, highly efficient BHJ photovoltaic cells with poly [N-9″-hepta-decanyl-2,7-carbazole-alt-5,5-(4′,7′-di-2-thienyl-2′,1′,3′-benzothiadiazole)] (PCDTBT) as the donor and [6]-phenyl $C_{70}$-butyric acid methyl ester ($PC_{70}BM$) as the acceptor (see Fig. 4.14) have been reported [119]. The PCDTBT/$PC_{70}BM$ solar cells exhibit one of the best performance of polymer solar cells studied to date, with PCE is 6.1 % and $V_{OC}$ is as high as 0.88 V. We performed simulations on the solar cells using the one-dimensional continuum device model.

It is essential to understand the fundamental processes of excitons and carriers governing photovoltaic conversion. Here we are interested in revealing the effect of e-h bound pair dissociation rate $k_d$ and recombination rate $k_f$ on $V_{OC}$. The PCDTBT/$PC_{70}BM$ solar cells exhibit one of the best performance of polymer solar cells studied to date, with $J_{SC} = 10.6$ mA cm$^{-2}$, $V_{OC} = 0.88$ V, $FF = 0.66$ and $\eta_e = 6.1$ %. The thickness of the active layer is 80 nm. The device is irradiated under both

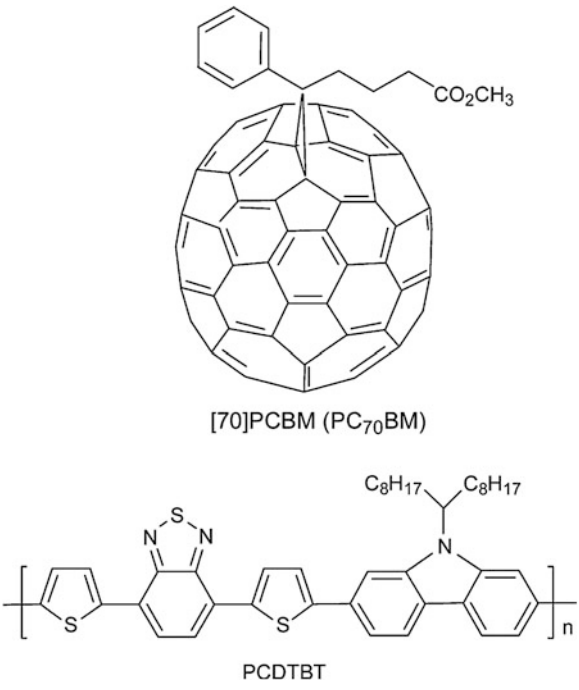


**Fig. 4.14** The chemical structures of $PC_{70}BM$ and PCDTBT

monochromatic green light (532 nm) with an intensity of 19.67 mW $cm^{-2}$ and AM 1.5 G with 100 mW $cm^{-2}$.

Firstly, the exciton generation rate $G$ is determined by the experimental optical absorption spectrum for the blend and the AM 1.5 G solar spectrum through the following equation:

$$G = \int_0^{800\text{nm}} (N_i(\lambda) - N_o(\lambda))d\lambda \Big/ L = \int_0^{800\text{nm}} (N_i(\lambda) \times (1 - 10^{-A(\lambda)\times L}))d\lambda \Big/ L \tag{4.60}$$

where $A$ is the normalized absorption coefficient, $\lambda$ is the photon wavelength, $N_i$ is the incident photon number per unit area, $N_o$ is transmitted photon number, $L$ is the thickness of the active layer of the solar cell.

For the BHJ structure, it is assumed that exciton generation is uniform, namely, the exciton generation is not space-dependent. Through (4.59), we obtain the rate as $G = 1 \times 10^{28}$ $m^{-3}$ $s^{-1}$ under AM 1.5 G radiations. The charge carrier mobilities are taken from the experimental measurements as $\mu_n = 3.5 \times 10^{-3}$ $cm^2$ $V^{-1}$ $s^{-19}$ and $\mu_p = 1.0 \times 10^{-3}$ $cm^2$ $V^{-1}$ $s^{-1}$ [120]. The dielectric constant $\varepsilon$ for conjugated polymers is typically between 3 and 4, here we set it to be 3.5. The effective density of states $N_c$ for electrons and holes at the electrodes is chosen to be $2.5 \times 10^{25}$ $m^{-3}$ [75]. The energy gap $E_{gap}$ between the LUMO of the acceptor and the HOMO of the donor is 1.3 eV, which sets the boundary condition for solving the Poisson equation.

It has been shown that $k_d$ depends on the electron-hole pair separation distance $a$ as well as on the built-in field and temperature [75, 109]. Here, we vary the electron-hole pair distance $a$ from 1 to 2.2 nm, which results in a range of $k_d$ from $10^5$ to $10^7$ $s^{-1}$. The decay rate $k_f$ is correspondingly varied from $10^5$ to $10^7$ $s^{-1}$. These values cover the practically accessible organic materials useful in photovoltaic cell applications. The simulated $V_{OC}$ versus $k_d$ and $k_f$ is shown in Fig. 4.15.

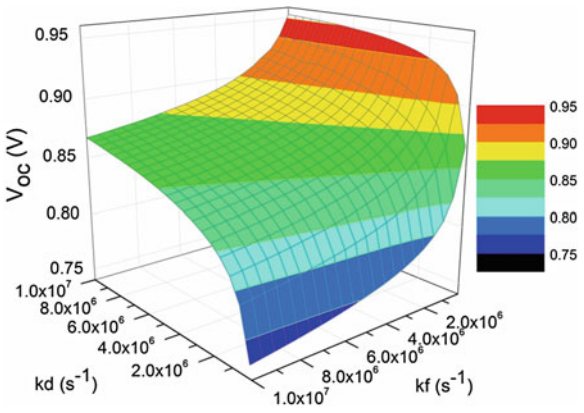


**Fig. 4.15** Influence of the dissociate rate $k_d$ and the decay rate $k_f$ on the open-circuit voltage $V_{OC}$ of the PCDTBT/$PC_{70}BM$ solar cells

For large open-circuit voltage $V_{OC} > 0.9$ V, which corresponds to a regime of $k_d > 4k_f$, as high as 79.1 % of the bound electron-hole pairs dissociate into free charge carriers without significant carrier decay to the ground state. In this case, a large number of free charge carriers could participate in the transport and reach the electrodes. In order to optimize the performance of organic solar cells, $V_{OC}$ as functions of several parameters are analyzed here. $V_{OC}$ is limited primarily by the effective band gap $E_{gap}$, namely, the gap between LUMO of acceptor and the HOMO of donor, and can be defined from the quasi-Fermi level splitting as [121]

$$eV_{OC} = E_{gap} - \underbrace{k_B T \ln\left(\frac{N_L N_H}{np}\right)}_{>0} \tag{4.61}$$

where $N_L$ and $N_H$ are the densities of states in the LUMO of the acceptor and HOMO of the donor respectively that cannot be exceeded by $n$ and $p$. Brabec et al. [121] presented experimental measurements showing an almost linear correlation of $V_{OC}$ with $E_{gap}$ for solar cells based on blends from polyphenylenevinylene with different fullerene derivatives.

For comparison, the experimental and simulated J-V curves under the illumination of both monochromatic green light (532 nm) and AM 1.5 G irradiation are simulated by device model in Fig. 4.16. The good agreement between the experiment and the simulation justifies the model adopted in our investigation and underlying mechanisms incorporated.

In Fig. 4.17, we present the result of light intensity effect on $V_{OC}$. $V_{OC}$ exhibits a straight line when plotted as a function of logarithm of light intensity. The fitted slope, 0.026 V is approximately equal to the experiment data $\sim$0.03 V conducted by Tromholt et al. [122] and consistent with the theoretical prediction based on the notion that the quasi-Fermi levels are constant throughout the device, as pointed out by Koster et al. [75].

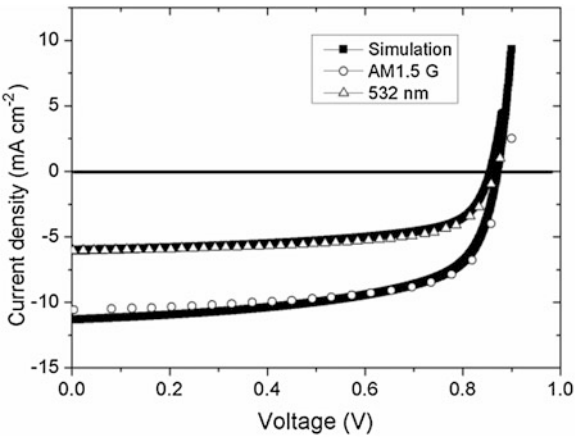


**Fig. 4.16** Comparison of the theoretical simulation of J-V curve with the experimental measurements for PCDTBT/$PC_{70}BM$ device. Two types of illumination condition are considered, AM 1.5 G and monochrome at 532 nm

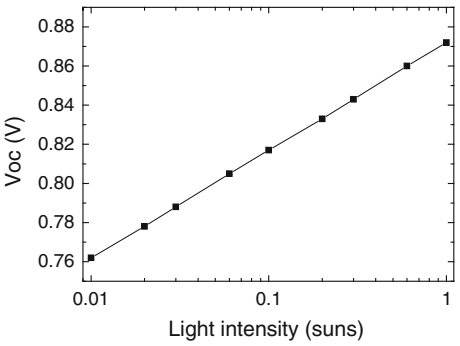


**Fig. 4.17** Light intensity dependence of $V_{OC}$ simulated by device model for the PCDTBT/$PC_{70}BM$ device

$$V_{oc} = \frac{E_{gap}}{q} - \frac{kT}{q}\ln\frac{(1-p)k_r N_c^2}{PG} \tag{4.62}$$

Namely, $V_{OC}$ is proportional to the logarithm of light intensity.

We further look at the effect of the charge carrier mobility on $V_{OC}$ as shown in Fig. 4.18. The increase in mobility leads to reduction of $V_{OC}$. Since the bimolecular recombination constant $k_r = \frac{\varepsilon}{q}\mu$, is proportional to the mobilities, and considering that recombination is a key loss mechanism, it is thus natural that high mobility results in high recombination rate. Hence the electron and hole density are reduced when large number of free charge carriers recombine throughout transport.

Last, we look at the charge mobility effects on short circuit current and the power conversion efficiency (Fig. 4.19). For the sake of comparison, we choose the all polymer device of the last section. It is seen that as the mobility increases, the short circuit current increases and then levels off, due to the steady current limit plus the

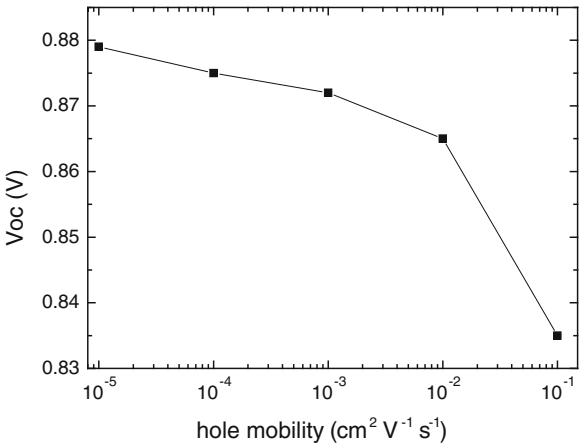


**Fig. 4.18** $V_{OC}$ as a function of hole mobility $\mu_p$ (the electron mobility $\mu_n$ is taken as 3.5 × $\mu_p$) simulated by device model for the PCDTBT/$PC_{70}BM$ device

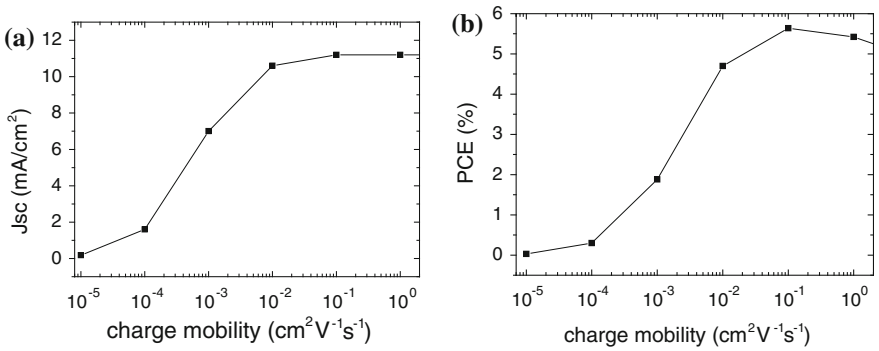


**Fig. 4.19** $J_{SC}$ (**a**) and PCE (**b**) as a function of charge mobility calculated for the all-polymer device

limited photo-generation of carriers. Similarly, the power conversion efficiency first increases, then levels off, and finally decreases, because the $V_{oc}$ decreases with charge mobility. This is in good agreement with previous studies [123, 124].

## 4.6 Conclusion and Outlook

In summary, we have presented progresses in theoretical modeling of the photovoltaic processes in polymer through computational studies, covering the optical absorption and emission spectra, as well as exciton decay processes associated with exciton migration, and the device performance. The performance is essentially determined by the corresponding chemical (or electronic) structures and physical morphologies. On one hand, some basic performance parameters depend critically on chemical compositions (or electronic structures) of organic solar cells, for instance, the short-circuit current $I_{SC}$ is actually constrained by the spectral light-harvesting ability of the constituent molecular semiconducting materials and their charge mobility; the open-circuit voltage $V_{OC}$ is linked directly to the quasi-Fermi level difference between the LUMO of acceptor and the HOMO of donor. Theoretical analyses are important in screening chemical structures to achieve better performance. Furthermore, electron dynamic based on electronic structures for describing elementary steps in photovoltaic process can now be quantum mechanically calculated, for instance, some theoretical advances in understanding exciton-related processes in organic photovoltaic materials have been illustrated in this chapter. So far, our understanding of exciton dynamics is limited to hopping picture. Quantum coherence effect should be considered for better understanding.

On the other hand, the physical morphology has also been demonstrated to be a key factor in determining the optoelectronic properties in organic devices. One can significantly improve the device performance by optimizing the nanoscale phase-

separation morphology: a large interfacial area is beneficial to both efficient exciton dissociation and charge transport channels all the way to the electrode for efficient charge collection. Numerical simulation tools, e.g., the dynamic Monte Carlo method and the continuum device model presented in this Chapter, indeed help to quantitatively analyze these morphology dependencies for photovoltaic performance.

As discussed above, the overall photovoltaic process modeling is a typical multiscale issue, thus the device performance is controlled by a series of complicated phenomena that span a wide range of length and time scales. As a consequence, only those theoretical simulation methods with multiscale characteristics can effectively describe the photovoltaic mechanism in organic solar cells.

Theoretical models at different scales (e.g., from first-principles methods to classical continuum medium calculations) could be integrated in "decoupled" or "coupled" schemes. The former usually refers that one can quantum mechanically calculate the electronic structures and some key dynamic processes of the concerned photovoltaic systems, and then these properties or parameters, classically numerical simulation methods could be well established. The latter mainly relies on effective information exchange between different models to realize a coupled simulation scheme. Commonly well-defined physical quantities by the involved theoretical models are usually exchanged as a bridge between different simulation models. These multiscale/multiphysics simulation methods are indispensable tools to optimize the design of functional organic optoelectronic materials in the future.

**Acknowledgments** The authors are indebted to Dr. Qian Peng and Dr. Yingli Niu for their contributions in the study of optical absorption/emission spectra and the excited state decays, and to Dr. Yuan Shang for his contribution to the continuum device model. The research in Shuai's group has been funded the National Natural Science Foundation of China, the Ministry of Science and Technology of China, and the Chinese Academy of Sciences.

## References

1. M. Pope, C.E. Swenberg, *Electronic Processes in Organic Crystals and Polymers*, 2nd edn. (Oxford University Press, New York, 1999)
2. E. Silinsh, V. Capek, *Organic Molecular Crystals: Interaction, Localization, and Transport Phenomena* (American Institute of Physics, New York, 1994)
3. H. Shirakawa, E.J. Louis, A.G. MacDiarmid, C.K. Chiang, A.J. Heeger, Chem. Commun. **578**, (1977)
4. W.P. Su, J.R. Schrieffer, A.J. Heeger, Phys. Rev. Lett. **42**, 1698 (1979)
5. J.L. Bredas, C. Adant, P. Tackx, A. Persoons, Chem. Rev. **94**, 243 (1994)
6. J.H. Burroughes, D.D.C. Bradley, A.R. Brown, R.N. Marks, K. Mackay, R.H. Friend, P.L. Burns, A.B. Holmes, Nature **347**, 539 (1990)
7. G. Gustafsson, Y. Cao, G.M. Treacy, F. Klavetter, N. Colaneri, A.J. Heeger, Nature **357**, 477 (1992)
8. F. Hide, M.A. Diaz-Garcia, B.J. Schwartz, M.R. Andersson, Q.B. Pei, A.J. Heeger, Science **273**, 1833 (1996)
9. N. Tessler, G.J. Denton, R.H. Friend, Nature **382**, 695 (1996)

10. S.V. Frolov, W. Gellemann, M. Ozaki, K. Yoshino, Z.V. Vardeny, Phys. Rev. Lett. **78**, 729 (1997)
11. G. Horowitz, Adv. Mater. **10**, 365 (1998)
12. H. Sirringhaus, P.J. Brown, R.H. Friend, M.M. Nielsen, K. Bechgaard, B.M.W. Langeveld-Voss, A.J.H. Spiering, R.A.J. Janssen, E.W. Meijer, P. Herwig, D.M. de Leeuw, Nature **401**, 685 (1999)
13. L. Kergoat, B. Piro, M. Berggren, G. Horowitz, M.C. Pham, Anal. Bioanal. Chem. **402**, 1813 (2012)
14. C. Brabec, V. Dyakonov, J. Parisi, N.S. Sariciftci (eds.), *Organic Photovoltaics* (Springer, Berlin, 2003)
15. R.E. Peierls, *Quantum Theory of Solids* (Oxford University Press, London, 1955)
16. A.J. Heeger, S. Kivelson, J.R. Schrieffer, W.P. Su, Rev. Mod. Phys. **60**, 781 (1988)
17. S.R. Marder, C.B. Gorman, F. Meyers, J.W. Perry, G. Bourhill, J.L. Bredas, B.M. Pierce, Science **265**, 632 (1994)
18. D. Moses, J. Wang, A.J. Heeger, N. Kirova, S. Brazovskii, Proc. Natl. Acad. Sci. U.S.A. **98**, 13496 (2001)
19. I. Hwang, G.D. Scholes, Chem. Mater. **23**, 610 (2011)
20. H. Ishii, K. Sugiyama, E. Ito, K. Seki, Adv. Mater. **11**, 605 (1999)
21. G. Yu, J. Gao, J.C. Hummelen, F. Wudl, A.J. Heeger, Science **270**, 1789 (1995)
22. N. Banerji, S. Cowan, M. Leclerc, E. Vauthey, A.J. Heeger, J. Am. Chem. Soc. **132**, 17459 (2010)
23. V. Coropceanu, J. Cornil, D.A. da Silva Filho, Y. Olivier, R. Silbey, J.L. Bredas, Chem. Rev. **107**, 926 (2007)
24. V. Lemaur, M. Steel, D. Beljonne, J.L. Bredas, J. Cornil, J. Am. Chem. Soc. **127**, 6077 (2005)
25. Y.P. Yi, V. Coropceanu, J.L. Bredas, J. Am. Chem. Soc. **131**, 15777 (2009)
26. J.L. Bredas, J.E. Norton, J. Cornil, V. Coropceanu, Acc. Chem. Res. **42**, 1691 (2009)
27. H. Bassler, Phys. Status Solidi B. **175**, 15 (1993)
28. P.W.M. Blom, M.J.M. de Jong, J.J.M. Vleggaar, Appl. Phys. Lett. **68**, 3308 (1996)
29. C. Tanase, E.J. Meijer, P.W.M. Blom, D.M. de Leeuw, Phys. Rev. Lett. **91**, 216601 (2003)
30. N. Vukmirovic, L.W. Wang, Nanolett. **9**, 3996 (2010)
31. P. Prins, F.C. Grozema, J.M. Schins, S. Patil, U. Scherf, L.D.A. Siebeles, Phys. Rev. Lett. **96**, 146601 (2006)
32. R.A. Street, J.E. Northrup, A. Salleo, Phys. Rev. B. **71**, 165202 (2005)
33. H. Sirringhaus, Adv. Mater. **17**, 2411 (2005)
34. H. Yan, Z. Chen, Y. Zheng, C. Newman, J. Quinn, F. Dotz, M. Kastler, A. Facchetti, Nature **457**, 679 (2009)
35. H.N. Tsao, D.M. Cho, I. Park, M.R. Hansen, A. Mavrinskiy, D.Y. Yoon, R. Graf, W. Pisula, H.W. Spiess, K. Muellen, J. Am. Chem. Soc. **133**, 2605 (2011)
36. L.J. Wang, G.J. Nan, X.D. Yang, Q. Peng, Q.K. Li, Z.G. Shuai, Chem. Soc. Rev. **39**, 423 (2010)
37. Z.G. Shuai, L.J. Wang, Q.K. Li, Adv. Mater. **23**, 1145 (2011)
38. A. Troisi, Chem. Soc. Rev. **40**, 2347 (2011)
39. S. Staftstrom, Chem. Soc. Rev. **39**, 2484 (2010)
40. R. Ianconescu, E. Pollak, J. Phys. Chem. **108**, 7778 (2004)
41. A.M. Mebel, M. Hayashi, K.K. Liang, S.H. Lin, J. Phys. Chem. A **103**, 10674 (1999)
42. Y.L. Niu, Q. Peng, C.M. Deng, X. Gao, Z.G. Shuai, J. Phys. Chem. A **114**, 7817 (2010)
43. C. Eckart, Phys. Rev. **47**, 552 (1935)
44. Q. Peng, Y.P. Yi, Z.G. Shuai, J.S. Shao, J. Chem. Phys. **126**, 114302 (2007)
45. Y.L. Niu, Q. Peng, Z.G. Shuai, Sci. China Ser. B- Chem. **51**, 1153 (2008)
46. M. Hayashi, A.M. Mebel, K.K. Liang, S.H. Lin, J. Chem. Phys. **108**, 2044 (1998)
47. J.Y. Kim, K. Lee, N.E. Coates, D. Moses, T.Q. Nguyen, M. Dante, A.J. Heeger, Science **2007**(317), 222 (2007)

48. N. Blouin, A. Michaud, M. Leclerc, Adv. Mater. **19**, 2295 (2007)
49. J. Hou, L.J. Huo, C. He, C.H. Yang, Y.F. Li, Macromolecule **39**, 4657 (2006)
50. I.W. Hwang, Q.H. Xu, C. Soci, B. Chen, A.K.Y. Jen, D. Moses, A.J. Heeger, Adv. Funct. Mater. **17**, 563 (2007)
51. B.S. Hudson, B.E. Kohler, E.C. Lim (eds.), *Excited States* (Academic, New York, 1973)
52. Z. Shuai, J.L. Bredas, S.K. Pati, S. Ramasesha, Phys. Rev. B **56**, 9298 (1997)
53. J.W.Y. Lam, B.Z. Tang, J. Polym. Sci. Part A Polym. Chem. **41**, 2607 (2003)
54. I. Gontia, S.V. Frolov, M. Liess, E. Ehrenfreund, Z.V. Vardeny, Phys. Rev. Lett. **82**, 4058 (1999)
55. D. Beljonne, Z.G. Shuai, L. Serrano-Andres, J.L. Bredas, Chem. Phys. Lett. **279**, 1 (1997)
56. L.P. Chen, X.J. Hou, L.Y. Zhu, S.W. Yin, Z.G. Shuai, J. Theo, Comput. Chem. **5**, 391 (2006)
57. Q. Peng, Y.L. Niu, Y.Q. Jiang, Y. Li, Z.H. Wang, Z.G. Shuai, J. Chem. Phys. **134**, 074510 (2011)
58. Y.Q. Jiang, Q. Peng, X. Gao, Z.G. Shuai, Y.L. Niu, S.H. Lin, J. Mater. Chem. **22**, 4491 (2012)
59. A.I. Krylov, Chem. Phys. Lett. **338**, 375 (2001)
60. O.V. Greitsenko, E.J. Baerends, Phys. Chem. Chem. Phys. **11**, 4640 (2009)
61. S. Grimme, M. Waletzke, J. Chem. Phys. **111**, 5645 (1999)
62. M. Liess, S. Jeglinski, P.A. Lane, Z.V. Vardeny, Synth. Met. **84**, 891 (1997)
63. L. Huo, T.L. Chen, Y. Zhou, J. Hou, H.-Y. Chen, Y. Yang, Y. Li, Macromolecules **42**, 4377 (2009)
64. J. Gierschner, H.-G. Mack, L. Luer, D. Oelkrug, J. Chem. Phys. **116**, 8596 (2002)
65. Z.G. Shuai, L.J. Wang, C.C. Song, *Theory of Charge Transport in Carbon Electronic Materials* (Springer, Heidelberg, 2012)
66. H. Wiesenhofer, D. Beljonne, G.D. Scholes, E. Hennebicq, J.L. Brédas, E. Zojer, Adv. Funct. Mater. **15**, 155 (2005)
67. B.P. Krueger, G.D. Scholes, G.R. Fleming, J. Phys. Chem. B. **102**, 5378 (1998)
68. D. Beljonne, J. Cornil, R.J. Silbey, P. Millié, J.L. Brédas, J. Chem. Phys. **112**, 4749 (2000)
69. S. Athanasopoulos, E. Hennebicq, D. Beljonne, A.B. Walker, J. Phys. Chem. C **112**, 11532 (2008)
70. E. Hennebicq, G. Pourtois, G.D. Scholes, L.M. Herz, D.M. Russell, C. Silva, S. Setayesh, A. C. Grimsdale, K. Müllen, J.L. Brédas, D. Beljonne, J. Am. Chem. Soc. **127**, 4744 (2005)
71. G.D. Scholes, Ann. Rev. Phys. Chem. **54**, 57 (2003)
72. C.P. Hsu, P.J. Walla, M. Head-Gordon, G.R. Fleming, J. Phys. Chem. B **105**, 11016 (2001)
73. C.P. Hsu, Z.Q. You, H.C. Chen, J. Phys. Chem. C **112**, 1204 (2008)
74. C.P. Hsu, Acc. Chem. Res. **42**, 509 (2009)
75. L.J.A. Koster, E.C.P. Smits, V.D. Mihailetchi, P.W.M. Blom, Phys. Rev. B **72**, 085205 (2005)
76. P.K. Watkins, A.B. Walker, G.L.B. Verschoor, Nano Lett. **5**, 1814 (2005)
77. D.T. Gillespie, J. Comput. Phys. **22**, 403 (1976)
78. L.Y. Meng, Y. Shang, Q.K. Li, Y.F. Li, X.W. Zhan, Z.G. Shuai, R.G.E. Kimber, A.B. Walker, J. Phys. Chem. B **114**, 36 (2010)
79. F. Yang, S.R. Forrest, ACS Nano **2**, 1022 (2008)
80. L.Y. Meng, D. Wang, Q.K. Li, Y.P. Yi, J.L. Bredas, Z.G. Shuai, J. Chem. Phys. **134**, 124102 (2011)
81. A.P.J. Jansen, Comput. Phys. Commun. **86**, 1 (1996)
82. J.J. Lukkien, J.P.L. Segers, P.A.J. Hilbers, R.J. Gelten, A.P.J. Jansen, Phys. Rev. E **58**, 2598 (1998)
83. R.A. Marsh, C. Groves, N.C. Greenham, J. Appl. Phys. **101**, 083509 (2007)
84. X. Zhan, Z.A. Tan, B. Domercq, Z. An, X. Zhang, S. Barlow, Y. Li, D. Zhu, B. Kippelen, S. R. Marder, J. Am. Chem. Soc. **129**, 7246 (2007)
85. J. Hou, Z.A. Tan, Y. Yan, C. He, C.H. Yang, Y. Li, J. Am. Chem. Soc. **128**, 4911 (2006)
86. R.A. Marcus, Rev. Mod. Phys. **65**, 599 (1990)
87. U. Wolf, V.I. Arkhipov, H. Baessler, Phys. Rev. B **59**, 7507 (1999)

88. V.I. Arkhipov, U. Wolf, H. Bässler, Phys. Rev. B **59**, 7514 (1999)
89. S. Barth, U. Wolf, H. Bässler, Phys. Rev. B **60**, 8791 (1999)
90. H.K. Gummel, IEEE Trans. Electron Devices **11**, 455 (1964)
91. M. Riede, T. Mueller, W. Tress, R. Schueppel, K. Leo, Nanotechnology **19**, 424001 (2008)
92. L.J.A. Koster, V.D. Mihailetchi, R. Ramaker, P.W.M. Blom, Appl. Phys. Lett. **86**, 123509 (2005)
93. S.M. Sze, *Physics of Semiconductor Devices* (Wiley, New York, 1981)
94. Y. Shang, Q. Li, L. Meng, D. Wang, Z. Shuai, Appl. Phys. Lett. **97**, 143511 (2010)
95. M. Casalegno, G. Raos, R. Po, J. Chem. Phys. **132**, 094705 (2010)
96. M.C. Scharber, D. Mühlbacher, M. Koppe, P. Denk, C. Waldauf, A.J. Heeger, C.J. Brabec, Adv. Mater. **18**, 789 (2006)
97. S. Selberherr, *Analysis and Simulation of Semiconductor Devices* (Spinger, New York, 1984)
98. B.K. Crone, P.S. Davids, I.H. Campbell, D.L. Smith, J. Appl. Phys. **87**, 1974 (2000)
99. B. Ruhstaller, S.A. Carter, S. Barth, H. Riel, W. Riess, J.C. Scott, J. Appl. Phys. **89**, 4575 (2001)
100. J.A. Barker, C.M. Ramsdale, N.C. Greenham, Phys. Rev. B **67**, 075205 (2003)
101. G.A. Buxton, N. Clarke, Phys. Rev. B **74**, 085207 (2006)
102. I. Hwang, N.C. Greenham, Nanotechnology **19**, 424012 (2008)
103. K. Maturova, M. Kemerink, M.M. Wienk, D.S.H. Charrier, R.A.J. Janssen, Adv. Funct. Mater. **19**, 1379 (2009)
104. K. Maturova, S.S. van Bavel, M.M. Wienk, R.A.J. Janssen, M. Kemerink, Nano Lett. **9**, 3032 (2009)
105. I. Hwang, C.R. McNeil, N.C. Greenham, J. Appl. Phys. **106**, 094506 (2009)
106. K. Maturova, R.A.J. Janssen, M. Kemerink, ACS Nano **4**, 1385 (2010)
107. J.T. Shieh, C.H. Liu, H.F. Meng, S.R. Tseng, Y.C. Chao, S.F. Horng, J. Appl. Phys. **107**, 084503 (2010)
108. Y.M. Nam, J. Huh, W.J. Jo, Sol. Energy Mater. Sol. Cells. **94**, 1118 (2010)
109. C.L. Braun, J. Chem. Phys. **80**, 4157 (1984)
110. L. Onsager, J. Chem. Phys. **2**, 599 (1934)
111. M. Wojcik, M. Tachiya, J. Chem. Phys. **130**, 104107 (2009)
112. P. Langevin, Ann. Chim. Phys. **28**, 433 (1903)
113. L.J.A. Koster, V.D. Mihailetchi, P.W.M. Blom, Appl. Phys. Lett. **88**, 052104 (2006)
114. G.J. Adriaenssens, V.I. Arkhipov, Solid State Commun. **103**, 541 (1997)
115. C. Deibel, A. Wagenpfahl, V. Dyakonov, Phys. Rev. B **80**, 075203 (2009)
116. G. Juska, K. Genevicius, N. Nekrasas, G. Sliauzys, R. Osterbacka, Appl. Phys. Lett. **95**, 013303 (2009)
117. M. Hilczer, M. Tachiya, J. Phys. Chem. C **114**, 6808 (2010)
118. J. Williams, A.B. Walker, Nanotechnology **19**, 424011 (2008)
119. S.H. Park, A. Roy, S. Beaupre, S. Cho, N. Coates, J.S. Moon, D. Moses, M. Leclerc, K. Lee, A.J. Heeger, Nat. Photonics **3**, 297 (2009)
120. S. Wakim, S. Beaupre, N. Blouin, B.R. Aich, S. Rodman, R. Gaudiana, Y. Tao, M. Leclerc, J. Mater. Chem. **19**, 5351 (2009)
121. C.J. Brabec, A. Cravino, D. Meissner, N.S. Sariciftci, T. Fromherz, M.T. Rispens, L. Sanchez, J.C. Hummelen, Adv. Funct. Mater. **11**, 374 (2001)
122. T. Tromholt, E.A. Katz, B. Hirsch, A. Vossier, F.C. Krebs, Appl. Phys. Lett. **96**, 073501 (2010)
123. M.M. Mandoc, L.J.A. Koster, P.W.M. Blom, Appl. Phys. Lett. **90**, 133504 (2007)
124. C. Deibel, A. Wagenpfahl, V. Dyakonov, Phys. Status Solidi-Rapid. Res. Lett. **2**, 175 (2008)